Enhancing the cooling performance of thermocouples

a power-constrained topology optimization procedure

Gutiérrez, G. Reales; Keulen, F. van; Goosen, J.F.L.; Aragón, A. M.; Bornheim, A.

Important note
To cite this publication, please use the final published version (if applicable).
Please check the document version above.

Enhancing the cooling performance of thermocouples: a power-constrained topology optimization procedure

G. Reales Gutiérrez[1] · F. van Keulen[1] · J. F. L. Goosen[1] · A. M. Aragón[1] · A. Bornheim[2]

Abstract

Heat pumping through thermoelectric devices has many advantages over traditional cooling. However, their current efficiency is a limiting factor in their implementation. In this paper, we approach the non-convex topology optimization of thermoelectrical elements for cooling applications through the method of moving asymptotes (MMA) to improve their cooling capabilities per watt usage. The optimization problem is defined for a given power budget, aiming for the minimum temperature with a known heat pumping need. The introduction of power as a constraint justifies the introduction of the voltage gradient across the thermocouple as a design variable to maintain the thermoelectrical device in its optimum power-to-heat extraction ratio. To better understand the convergence of this non-convex problem, we present a two-variable analytical thermoelectric optimization model. This example provides information on how to select the penalty parameters used to scale the three material coefficients involved in the problem to obtain lower objective values and better convergence using MMA. The analytical model shows the non-convexity of the problem and provides the recommendation to use penalization coefficients of the form $p_k = p_\sigma > p_\alpha = 1$ for the thermal conductivity, electrical conductivity, and Seebeck coefficients. We tested these penalization coefficients through optimizations of a model based on the 1MC10-031 commercial thermoelectric-cooler (TEC) using the finite element method (FEM). These penalization coefficients provided local minima without the need for volume constraints. With this procedure, we found designs that provided temperatures close to 10 degrees lower using 60% less semiconductor material volume compared to the initial design.

Keywords Topology optimization · Thermoelectric-cooler (TEC) · Power constraint · Temperature minimization · SIMP · Non-convexity

1 Introduction

The energy consumption for cooling and heating accounts for half of the global energy consumption and 40% of global energy-related CO_2 emissions, respectively (IRENA et al. 2020). Most heat-transfer related activities are carried out through compressor- and refrigerant-based systems for active thermal management. Conversely, thermoelectric modules offer an alternative thermal management solution with simpler static systems, higher reliability, lower maintenance cost, refrigerant-free operation (Liu et al. 2022b), miniaturization possibilities, and reverse heat-pumping capabilities (Riffat and Ma 2003). These advantages make thermoelectric-coolers (TECs) ideal for niche applications such as sustainable self-cooling, cryogenic applications, medical, food or building refrigeration, thermal cycling and electronic cooling of sensors, lasers, and chips (Zhao and Tan 2014). Despite their advantages over conventional systems, TECs have yet to see a significant adoption in applications where they compete against turbomachinery-based cooling systems due to their low energy conversion efficiency and high system cost (approximately $75 W^{-1} (LeBlanc et al. 2014) per TEC against $7 W^{-1} for liquid electronic cooling systems (Maurya 2020).

The static behavior and miniaturization possibilities of TECs arise from using the Peltier effect. First observed in

✉ G. Reales Gutiérrez
g.realesgutierrez@tudelft.nl

1   Faculty of Mechanical Engineering, Delft University of Technology, Mekelweg 2, 2628 CD Delft, The Netherlands

2   California Institute of Technology, High Energy Physics 1200 E California Blvd, Pasadena, CA 91125, USA

1834 (Peltier 1834), the Peltier effect dictates that when a current is passed through two dissimilar conductors, such as a p–n semiconductor junction, heat absorption occurs at the interface, arising from the elevation of the energy levels of electrical current electrons from the p-type to the n-type semiconductor. The Seebeck effect can also be harnessed through dissimilar conductor connections, called thermocouples, to generate an electrical potential gradient, which can be harnessed for applications such as heat recovery and power generation in remote or hard-to-reach locations. Peltier and Seebeck effects exists within the same thermoelectric device architecture based on thermocouples.

As the smallest unit of thermoelectric device architecture, the thermocouple has captured significant attention in endeavors aimed at improving the efficiency of thermoelectric devices. On the one hand, these efforts focus on reconciling the conflicting material properties of the often used semiconductor materials. To have high efficiency, we require high electrical conductivity, low thermal conductivity, and large Seebeck coefficient gradients—related by the Wiedemanne–Franz law—to maximize the figure of merit or *ZT*, directly associated with the device's efficiency. These properties can be modified through the nanoscale constituents of semiconductors; however, the procedures required are limited by the available material composition and manufacturing technologies, with the largest *ZT* obtained being in the range of 1–3 (Zhao and Tan 2014). On the other hand, the electrical and thermal conductivities of the entire device also depend on the thermocouple topology. Numerical simulations show that thermocouples with variable cross-sections can provide higher efficiencies and lower stresses than conventional constant section thermocouples (Ibeagwu 2019). In particular, thermocouple design is highly interesting for the standard thermoelectrical module architecture (flat-bulk) (He et al. 2018). Fabián-Mijangos et al. (2017) experimentally tested multiple thermocouple designs, showing efficiency increases using asymmetric thermocouples for power recovery.

Topology optimization (TO) is a powerful tool for enhancing the efficiency of thermocouples without the need for extensive experimental testing and its associated costs. Since its inception with Bendsøe and Kikuchi (1988), the method has promoted different variations such as the commonly used solid isotropic material with penalization (SIMP) or level set (LS) approaches, among others (Yago et al. 2021; Sigmund and Maute 2013). TO is practical for designing thermoelectrical compliant microactuators, showing promise with both SIMP and LS approaches (Mativo and Hallinan 2019; Furuta et al. 2017; Sardan et al. 2008). Additionally, TO can increase the efficiency of heat recovery devices using novel thermocouple designs (Takezawa and Kitamura 2012) and multi-material optimizations (Xu et al. 2019). Finally, Soprani et al. (2016) delve into the

optimization of thermal coupling materials for TECs and Lundgaard and Sigmund (2018) looks into the topology optimization of multi-material thermoelectrical devices for multiple objective criteria.

Despite research on TO applied to thermoelectric-compliant mechanisms and heat recovery, current formulations fall short regarding cooling applications and specific working points. A more tailored TO formulation that takes TEC design considerations into account can provide a reduction of bulk-material costs (representing approximately 1/3 of the system cost according to LeBlanc et al. (2014)) and improved cooling performance. Furthermore, previous formulations have overlooked important operational factors, such as the working points for electrical and power consumption and their limitations. The lack of attention to these factors often leads to postprocessing at different operational points to understand the device's actual performance, (Lundgaard and Sigmund 2018). Furthermore, the lack of study of the multiple electrical working points neglects the effect of the nonlinear Joule heating over the topology of the device. Previous results for heat recovery also tend to use volume constraints, which reduce the performance of the designs studied (Mativo et al. 2020; Takezawa and Kitamura 2012). Furthermore, in thermoelectrical devices, increasing the volumes of semiconductor material in the design does not necessarily lead to better performances (Shittu et al. 2020). This fact raises doubts about the optima found using volume constraints. Additionally, the absence of thermoelectrical optimization results based on 3D geometries in the literature raises questions about the influence of intricate geometries on the design of each semiconductor leg, or pellet, in a thermocouple.

This paper presents a novel approach to optimize three-dimensional TEC thermocouples using topology optimization. First, we propose an analytical model with two design variables to study the design space and understand its non-convexity. This model is studied concerning the material scaling used in SIMP to predict the optimization parameters to improve the convergence of an optimization problem with a larger number of design variables. Secondly, we apply TO to a finite element model of a thermocouple based on a commercial product, validating the insights from the lower-dimensionality problem. These models are studied with constant material properties to compare with the analytical solution of the thermoelectrical equations. Using constant materials further reduces the computational complexity and cost of the models. We later study the error introduced by these assumptions in the results section. Furthermore, the design considerations of TECs are integrated into the optimization through the selection of a temperature objective function subject to power consumption limitations. In this model, the power consumption can be modified through the density design variables and the voltage gradient through the thermocouples. This voltage design variable

introduces an electrical control over the nonlinear Joule heating in the device. Finally, the results are studied for multiple electrical and thermal working points of the thermocouple.

2 Governing equations

The bulk-flat thermoelectrical architecture depicted in Fig. 1 uses alternating p- and n-type pellet-shaped thermoelectric materials connected electrically in series and thermally in parallel. Copper layers on the top and bottom of each thermoelectric leg serve as electrical contacts, and two ceramic plates provide thermal contacts. Although all the materials in the thermoelectrical modeling should account for all three elements, the Seebeck coefficients of the copper layers are often neglected due to symmetry conditions, with only thermal degrees of freedom. However, the bulk properties of the semiconductors are subject to nonlinear thermoelectric coupling.

Goupil et al. (2011) provides the balance and constitutive equations representing the thermoelectrical coupling. We can write down the balance equations in stationary conditions for the electric charge and energy flux as

$$
\begin{aligned}
\nabla \mathbf{j} &= 0, \\
\nabla \mathbf{q} + \mathbf{j} \cdot \nabla \phi &= q_{\Omega},
\end{aligned} \tag{1}
$$

where $\mathbf{j}$ is the current density, $\mathbf{q}$ is the heat flow, q_{Ω} is the heat generated in the volume, and ϕ is the electrical potential across the semiconductor material. These equations then express—within a given volume—the conservation of internal charge and energy given their flow through the volume boundary without magnetic fields.

The Ohm and Fourier equations,

$$
\mathbf{j} = -\sigma(\nabla \phi + \alpha \nabla T), \tag{2}
$$

$$
\mathbf{q} = \alpha T \mathbf{j} - k \nabla T, \tag{3}
$$

complete the thermoelectrical coupling. Where σ is the electrical conductivity, α is the Seebeck coefficient, k is the

thermal conductivity of the semiconductor material, and T is its temperature. Equations (2) and (3) provide the constitutive equations and a relation between the temperature, heat flux, electrical potential and current flow. Although we can analytically solve these equations for simple configurations, complex geometries or nonlinear material properties can only be solved numerically.

2.1 Finite element modeling

The thermoelectric equations' finite element formulation makes it possible to solve complex semiconductor topologies. With Eqs. (1)–(3) as the strong formulation of the thermoelectric problem, we need to introduce the required boundary conditions to solve it. We can write these boundary conditions as

$$
\begin{aligned}
V &= V_{\Gamma_V} \text{ in } \Gamma_V, & T &= T_{\Gamma_V} \text{ in } \Gamma_V, \\
\mathbf{j} \cdot \mathbf{n} &= j_c \text{ in } \Gamma_j, & \mathbf{q} \cdot \mathbf{n} &= q_c \text{ in } \Gamma_q,
\end{aligned} \tag{4}
$$

where V_{Γ_V} and T_{Γ_V} define the prescribed degrees of freedom in the domain, and q_c and j_c represent the externally prescribed heat flows and current densities, respectively. The defined boundaries satisfy the conditions $\Gamma_V \cup \Gamma_j = \Gamma, \Gamma_V \cap \Gamma_j = 0$ where Γ represents the entire boundary. Similarly, the thermal boundaries satisfy $\Gamma_T \cup \Gamma_q = \Gamma, \Gamma_T \cap \Gamma_q = 0$.

The thermoelectrical system can now be transformed into the weak form of the Eqs. (1)–(3), using an approximation function ω and the divergence theorem,

$$
\begin{aligned}
&-\int_{\Omega} \omega \nabla \mathbf{q} \, d\Omega + \int_{\Omega} \omega \mathbf{j} \cdot \nabla \phi \, d\Omega + \int_{\Gamma_q} \omega q_c \, d\Gamma \\
&= \int_{\Omega} \omega q_{\Omega} \, d\Omega, \\
&-\int_{\Omega} \nabla \omega \cdot \mathbf{j} \, d\Omega + \int_{\Gamma_j} \omega \cdot \mathbf{j_c} \, d\Gamma = 0.
\end{aligned} \tag{5}
$$

We can now discretize Eq. (5) to reach the Garlekin formulation using the approximation shape functions as,

$$
\begin{aligned}
T &= \mathbf{N}^{\mathsf{T}} \mathbf{T}, \\
\phi &= \mathbf{N}^{\mathsf{T}} \mathbf{V},
\end{aligned} \tag{6}
$$

where $\mathbf{V}$ and $\mathbf{T}$ are the temperature and voltage degrees of freedom and $\mathbf{N}$ contains the shape functions. Combining Eq. (6) with Eq. (5) and creating a homogeneous equation system, we obtain the residual ($\mathbf{R}$) for a given nodal value solution,
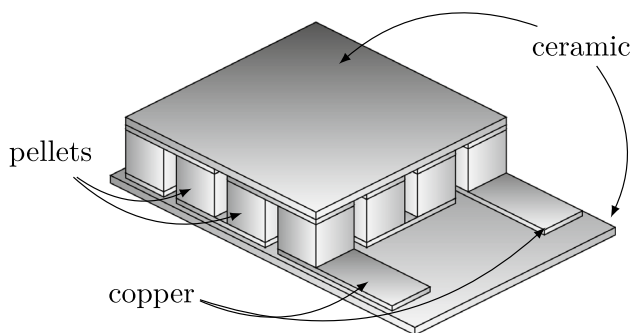
Fig. 1 Flat-bulk thermoelectric-cooler (TEC) schematic exemplifying the electrical contacts between the semiconductor pellets and the thermal contact plates

$$\mathbf{R} = \begin{bmatrix} \mathbf{R_A} \\ \mathbf{R_B} \end{bmatrix},$$

$$\mathbf{R_A} = -\int_{\Omega} \mathbf{N}\boldsymbol{\nabla}\mathbf{q}\,\mathrm{d}\Omega + \int_{\Omega} \mathbf{N}\mathbf{j}\cdot\boldsymbol{\nabla}\mathbf{N}^{\mathsf{T}}\mathbf{V}\,\mathrm{d}\Omega$$
$$+\int_{\Gamma_q} \mathbf{N}q_c\,\mathrm{d}\Gamma - \int_{\Omega} \mathbf{N}q_{\Omega}\,\mathrm{d}\Omega = \mathbf{0}, \tag{7}$$

$$\mathbf{R_B} = -\int_{\Omega} \boldsymbol{\nabla}\mathbf{N}\cdot\mathbf{j}\,\mathrm{d}\Omega + \int_{\Gamma_j} \mathbf{N}\cdot\mathbf{j_c}\,\mathrm{d}\Gamma = \mathbf{0}.$$

We can separate this residual into its components related to the temperature, $\mathbf{R_A}$, and voltage, $\mathbf{R_B}$, degrees of freedom. PérezAparicio et al. (2007) provides a more detailed development of the thermoelectric finite element method (FEM) equations with benchmark tests concerning analytical solutions and nonlinear material properties.

To obtain the solution of this system, we use the Newton–Raphson algorithm with the tangent system matrix, $\mathbf{K^k}$, calculated for each iteration and equal to the derivative of the residual concerning the problem degrees-of-freedom;

$$\mathbf{K^k} = \begin{bmatrix} \dfrac{\partial \mathbf{R^k}}{\partial \mathbf{T}} & \dfrac{\partial \mathbf{R^k}}{\partial \mathbf{V}} \end{bmatrix} = \begin{bmatrix} \dfrac{\partial \mathbf{R_A^k}}{\partial \mathbf{T}} & \dfrac{\partial \mathbf{R_A^k}}{\partial \mathbf{V}} \\ \dfrac{\partial \mathbf{R_B^k}}{\partial \mathbf{T}} & \dfrac{\partial \mathbf{R_B^k}}{\partial \mathbf{V}} \end{bmatrix}. \tag{8}$$

We can expand the derivatives of the residual to an integral form for any given iteration,

$$\frac{\partial \mathbf{R_A}}{\partial \mathbf{T}} = -\int_{\Omega} \boldsymbol{\nabla}\mathbf{N}\frac{\partial \mathbf{q}}{\partial \mathbf{T}}^{\mathsf{T}}\,\mathrm{d}\Omega + \int_{\Omega} \mathbf{N}(\frac{\partial \mathbf{j}}{\partial \mathbf{T}}^{\mathsf{T}}\boldsymbol{\nabla}\mathbf{N}^{\mathsf{T}}\mathbf{V})^{\mathsf{T}}\,\mathrm{d}\Omega,$$

$$\frac{\partial \mathbf{R_A}}{\partial \mathbf{V}} = -\int_{\Omega} \boldsymbol{\nabla}\mathbf{N}\frac{\partial \mathbf{q}}{\partial \mathbf{V}}^{\mathsf{T}}\,\mathrm{d}\Omega + \int_{\Omega} \mathbf{N}(\frac{\partial \mathbf{j}}{\partial \mathbf{V}}^{\mathsf{T}}\boldsymbol{\nabla}\mathbf{N}^{\mathsf{T}}\mathbf{V})^{\mathsf{T}}\,\mathrm{d}\Omega$$
$$+\int_{\Omega} \mathbf{N}(\mathbf{j}^{\mathsf{T}}\boldsymbol{\nabla}\mathbf{N})^{\mathsf{T}}\,\mathrm{d}\Omega, \tag{9}$$

$$\frac{\partial \mathbf{R_B}}{\partial \mathbf{T}} = -\int_{\Omega} \boldsymbol{\nabla}\mathbf{N}\frac{\partial \mathbf{j}}{\partial \mathbf{T}}^{\mathsf{T}}\,\mathrm{d}\Omega,$$

$$\frac{\partial \mathbf{R_B}}{\partial \mathbf{V}} = -\int_{\Omega} \boldsymbol{\nabla}\mathbf{N}\frac{\partial \mathbf{j}}{\partial \mathbf{V}}^{\mathsf{T}}\,\mathrm{d}\Omega,$$

These equations depend on the heat and current flow derivatives. Using constant material properties with the temperature, we can write the equations as follows:

$$\frac{\partial \mathbf{j}}{\partial \mathbf{V}} = -\sigma\boldsymbol{\nabla}\mathbf{N}^{\mathsf{T}},$$

$$\frac{\partial \mathbf{j}}{\partial \mathbf{T}} = -\alpha\sigma\boldsymbol{\nabla}\mathbf{N}^{\mathsf{T}},$$

$$\frac{\partial \mathbf{q}}{\partial \mathbf{V}} = \alpha(\mathbf{N}^{\mathsf{T}}\mathbf{T})\frac{\partial \mathbf{j}}{\partial \mathbf{V}}, \tag{10}$$

$$\frac{\partial \mathbf{q}}{\partial \mathbf{T}} = \alpha(\mathbf{N}^{\mathsf{T}}\mathbf{T})\frac{\partial \mathbf{j}}{\partial \mathbf{V}} + \alpha\mathbf{j}\mathbf{N}^{\mathsf{T}} - k\boldsymbol{\nabla}\mathbf{N}^{\mathsf{T}}.$$

Notice that simplifying the material description using non-temperature-dependent material properties reduces the

complexity of the TO. However, the lack of material nonlinearities disregards the Thomson effect. The Thomson effect relates to the gradient of the Seebeck coefficient with the temperature and induces an extra component in the electrical current flow. However, this effect is small compared to the other thermoelectric effects and can be ignored (Lee 2013). Disregarding the Thomson effect implies that the results are inaccurate for large temperature deviations from the temperature point used to measure the material properties (Sandoz-Rosado et al. 2013).

The nonlinearities in the problem, arising from the strong coupling of the thermoelectrical equations and subsequent Joule heating, can produce convergence issues within the NR. Higher-order elements provide exact results for the second-order thermoelectric equations within each element, improving convergence. Using higher-order elements also increases the overall computational complexity of the problem. However, the nanometer validity limit for the thermoelectrical equations and manufacturability limitations to micrometer level (Liu et al. 2022a) reduce the element and system size we need to solve. Using a filter to set a characteristic length scale could also mitigate these effects at the cost of higher complexity. To reduce the computational cost of the higher-order element, we use 20 node serendipity elements and a 14 point integration scheme based on integration locations in the corners and faces of a hexahedron internal to the element. Hoit and Krishnamurthy (1995) describes the advantages and development of this integration scheme with benchmark examples, and the whole element and integration implementation can be found in Sect. A.

3 Optimization formulation

The optimization algorithm employed in this work follows that proposed first by Bendsøe and Kikuchi (1988). The design variables x_e represent a variation of the density of the element associated with it,

$$\rho_e(x_e) = x_e\rho_0, \tag{11}$$

where ρ_e is the density of element e dependent on its design variable, and ρ_0 is the nominal density of the material associated with that element. We define the rest of the material properties with respect to the design variable x_e with a penalty coefficient as,

$$\alpha_e = \alpha_{\min} + x_e^{p_\alpha}(\alpha_0 - \alpha_{\min}),$$
$$k_e = k_{\min} + x_e^{p_k}(k_0 - k_{\min}), \tag{12}$$
$$\sigma_e = \sigma_{\min} + x_e^{p_\sigma}(\sigma_0 - \sigma_{\min}),$$

where we interpolate between the minimum allowed value, denoted by the subindex min, and the nominal value of the semiconductor material, denoted by the subindex 0. This

interpolation helps to avoid numerical singularities at each linear solve of the Newton–Raphson iterations. Furthermore, the penalization coefficient p_i for each material property helps to avoid intermediate-density results, rapidly decreasing the influence of each variable at lower densities.

Once we have defined the material properties concerning our design variables, we can define the objectives and constraints of our optimization from the problem's governing equations. Traditionally, the objective function for thermoelectric devices is their efficiency, which involves the ratio of the heat extracted against the power consumption, defined as the coefficient-of-performance (COP) for a heat pumping device,

$$\text{COP} = \frac{Q[W]}{P[W]}, \tag{13}$$

where Q is the heat extracted by the TEC and P is its power consumption, whose ratio will always be higher than 1. Knowing the power dissipation of the electronic system we want to cool down, we know the heat extracted Q. Fixing Q limits a COP maximization objective to reduce power consumption and increase device efficiency. However, reducing power consumption for a known heat extraction does not necessarily correlate to a lower temperature in our electronics, which is critical for specific applications (Bornheim et al. 2023). Defining the electronics temperature as our optimization objective means that we must include the power limitation—or power budget—of the thermoelectric system as a constraint, as it is no longer present in our objective function.

As we can easily modify the power consumption by external operational inputs—applied voltage or current through the device—to work on more efficient states, we must include this operation in the optimization to compare to the initial design. For this purpose, we introduce an externally applied voltage boundary condition as a design variable. This voltage allows us to compare the optimum working point of the non-optimized designs without postprocessing. Furthermore, the voltage gradient design variable considers the system's nonlinear behavior concerning the applied electrical load.

In some cases, reducing the volume does not improve the TEC's performance. If we still want to limit the material used and associated costs, we must introduce a volume constraint to the problem.

The optimization shall take into account the objective and constraints as

$$\mathbf{x} = \arg\min_{\mathbf{x}} \; : T_{avg}(\mathbf{x}, \mathbf{U}) = \frac{1}{n_n} \sum_{i=1}^{n_n} (T_i) = \mathbf{L}^{\mathsf{T}} \mathbf{U}, \tag{14a}$$

subject to: $\mathbf{R^k} = \mathbf{0}$, $\tag{14b}$

$$c_v = \sum_{e=1}^{n_e} \frac{v_e x_e}{v_0 v_{obj}} - 1 \le 0, \tag{14c}$$

$$c_P = \frac{P}{P_{obj}} - 1 < 0, \tag{14d}$$

$$V_f = V_{\min} + x_{n_e+1}(V_{\max} - V_{\min}), \tag{14e}$$

where the objective function, T_{avg}, is defined as the average temperature value of the specified nodal values. Only the nodal values of the surface of the thermocouple in contact with the device to cool down—in this case, one of the copper interfaces—need to be taken into account for the objective value, with n_n being the total number of nodes in this surface. This summation can then be represented as a matrix product of a vector of constant values ($\mathbf{L}$)—equal to $\frac{1}{n_n}$ for the nodal temperature values within the surface to cool down and zero otherwise—by the vector $\mathbf{U}$ that contains the nodal degrees of freedom (DOFs). For this calculation to be accurate, after the optimization has converged, we need to ensure that the temperature DOFs at the copper surface temperature have a uniform value.

Furthermore, the established limit volume for optimization, v_{obj}, and design variables, $\mathbf{x}$, are scaled between 0 and 1. The volume constraint, Eq. (14c), is calculated dependent on each element design variable, x_e, related to the total initial design volume, v_0, and the desired maximum volume percentage, v_{obj}. While the power consumption constraint, Eq. (14d), can surpass a value of 1, it is made dimensionless with the limiting power budget, P_{obj}. If both values are of the same order of magnitude, the optimization should not be affected.

To calculate the overall power consumption, we need to define the power differential as the current density multiplied by the differential of the voltage gradient at a given point. We can calculate the total power consumption of the thermocouple through the sum of the volume integral of this power differential for each element as

$$P = \sum_{e=1}^{n_e} P_e = \sum_{e=1}^{n_e} \left(-\int_{\Omega_e} \mathbf{j}^{\mathsf{T}} \mathbf{\nabla N}^{\mathsf{T}} \mathbf{V_e} \, d\Omega_e \right), \tag{15}$$

where n_e is the total number of elements in the FEM model, Ω_e the volume associated with a given element with e denoting element-based properties, and the minus sign takes into account the opposite sense of the current and voltage differentials.

To be able to maintain the optimal power consumption for any x_e density design space, within our power budget

limitations, we introduce an extra design variable x_{n_e+1} stored in the last index of the design variable vector $\mathbf{x}$ of size $n_e + 1$. This variable is related to the voltage boundary condition (V_f) through a linear interpolation, Eq. (14e), between user-selected voltage values ($V_{\max}, V_{\min}$). As stated in the objective and design variable discussion, this variable introduces the nonlinear dependency of the power consumption and Joule heating into the problem. Using x_{n_e+1} as a design variable allows, the thermoelectrical pellet, to work at the optimum electrical load during the optimization, reducing the postprocessing needs to study different working points and avoiding lower efficiencies due to high current density concentrations at higher electrical loading.

We can now solve this problem with the method of moving asymptotes (MMA) (Svanberg 1987) optimization algorithm. MMA is popular in the structural optimization field due to its robustness, flexibility, and ability to handle multiple constraints even if other optimization algorithms provide better computational efficiency (Yang and Yang 2010; Fanni et al. 2013). MMA is based on specific convex functions' local approximation of the nonlinear problem. These approximations require the derivative of the objective and constraint equations concerning the design variables x_e that are calculated in each iteration of MMA.

Subsequently, each MMA step needs to recalculate the FEM solution running an NR algorithm from a given initial point. Using the linearized equations concerning the nodal degrees of freedom, Eqs. (8)–(10), we find that certain conditions for the NR initial point can improve the convergence of the method:

- For the first step of the MMA algorithm, without information on previous NR solutions,

$$\mathbf{T} = \mathbf{0}, \quad \mathbf{V} = \mathbf{0}, \tag{16}$$

  provides convergent solutions if the boundary conditions are not electrically or thermally disconnected.
- Having a solution from a previous MMA step, we can improve the NR convergence rate using the initial point,

$$\mathbf{T}^{t+1} = \mathbf{T}^t, \quad \mathbf{V}^{t+1} = \mathbf{V}^t \frac{V_f^{t+1}}{V_f^t}. \tag{17}$$

  where t represents the ith step of the MMA procedure.

3.1 Sensitivity calculation

In this section, we separate the problem, Eq. (14), into each of its objectives and constraints to calculate their derivatives concerning the design variables. We can use these sensitivities to find an optimum thermocouple design through gradient descent optimization algorithms.

3.1.1 Objective function

The objective function defined in Eq. (14a) defines the average temperature from the surface of the thermocouple in charge of extracting heat from the environment. From this equation, we can apply the adjoint theorem to calculate its derivatives using an equivalent objective defined as,

$$T_{avg}^* = \mathbf{L}^\mathsf{T}\mathbf{U} + \mathbf{\Lambda}^\mathsf{T}\mathbf{R}^k,$$

where we include the residuals from the thermoelectric system solution, which tends to zero for convergence conditions of the Newton–Raphson algorithm, multiplied by a vector of unknown constants $\mathbf{\Lambda}$. We can write the derivative of this new expression of the objective function concerning the design variables as,

$$\frac{\mathrm{d}T_{avg}^*}{\mathrm{d}\mathbf{x}} = \mathbf{L}^\mathsf{T}\frac{\mathrm{d}\mathbf{U}}{\mathrm{d}\mathbf{x}} + \mathbf{\Lambda}^\mathsf{T}\left(\frac{\mathrm{d}\mathbf{R}^k}{\mathrm{d}\mathbf{x}}\right). \tag{18}$$

Considering the dependencies of each variable and the values of the prescribed degrees of freedom ($\bar{\mathbf{U}}$), we can write

$$\begin{aligned}&\mathbf{R}^k = R(U, \bar{\mathbf{U}}, x)\\&\mathbf{U} = \mathbf{U}(\mathbf{x}, V_f); \bar{\mathbf{U}} = \bar{\mathbf{U}}(V_f),\\&V_f = V_f(x_{n_e+1}),\end{aligned} \tag{19}$$

and applying the chain rule to the residual derivative, we get

$$\frac{\mathrm{d}\mathbf{R}^k}{\mathrm{d}\mathbf{x}} = \frac{\partial\mathbf{R}^k}{\partial\mathbf{x}} + \mathbf{K}^\mathbf{k}\left(\frac{\partial\bar{\mathbf{U}}}{\partial V_f}\frac{\mathrm{d}V_f}{\mathrm{d}\mathbf{x}} + \frac{\mathrm{d}\mathbf{U}}{\mathrm{d}\mathbf{x}}\right). \tag{20}$$

We can then write the derivative of the average temperature as

$$\begin{aligned}\frac{\mathrm{d}T_{avg}^*}{\mathrm{d}\mathbf{x}} =&(\mathbf{L}^\mathsf{T} + \mathbf{\Lambda}^\mathsf{T}\mathbf{K}^\mathbf{k})\frac{\mathrm{d}\mathbf{U}}{\mathrm{d}\mathbf{x}}\\&+ \mathbf{\Lambda}^\mathsf{T}\left(\frac{\partial\mathbf{R}^k}{\partial\mathbf{x}} + \mathbf{K}^\mathbf{k}\frac{\partial\bar{\mathbf{U}}}{\partial V_f}\frac{\mathrm{d}V_f}{\mathrm{d}\mathbf{x}}\right),\end{aligned} \tag{21}$$

and we obtain the adjoint equation so that the components multiplying a derivative of $\mathbf{U}$ concerning a design variable is zero,

$$\mathbf{\Lambda} = -(\mathbf{K}^\mathbf{k})^{-\mathsf{T}}\mathbf{L}. \tag{22}$$

Substituting Eq. (22) into Eq. (21), we can now calculate the derivatives concerning the design variables,

$$\frac{\mathrm{d}T_{avg}^*}{\mathrm{d}\mathbf{x}} = +\mathbf{\Lambda}^\mathsf{T}\left(\frac{\partial\mathbf{R}^\mathsf{T}}{\partial\mathbf{x}} + \mathbf{K}^\mathbf{k}\frac{\partial\bar{\mathbf{U}}}{\partial V_f}\frac{\mathrm{d}V_f}{\mathrm{d}\mathbf{x}}\right), \tag{23}$$

where this solution can be reduced to the element level taking into account that each element depends only on each density design variable x_e, and we can treat x_{n_e+1}, which

modifies the voltage boundary conditions separately. We can calculate the sensitivity concerning a x_e density design variable as,

$$\frac{\mathrm{d}T^*_{avg}}{\mathrm{d}x_e} = \mathbf{\Lambda}^\mathsf{T}_e \frac{\partial \mathbf{R}^k}{\partial x_e}, \tag{24}$$

where the derivatives of the residual can be written in an integral form using the element densities,

$$\frac{\partial \mathbf{R^k_A}}{\partial x_e} = -\int_{\Omega_e} \boldsymbol{\nabla}\mathbf{N}\frac{\partial \mathbf{q}}{\partial x_e}^\mathsf{T} \mathrm{d}\Omega_e + \int_{\Omega_e} \mathbf{N}(\frac{\partial \mathbf{j}}{\partial x_e}^\mathsf{T} \boldsymbol{\nabla}\mathbf{N}^\mathsf{T}\mathbf{V})^\mathsf{T} \mathrm{d}\Omega_e,$$

$$\frac{\partial \mathbf{R^k_B}}{\partial x_e} = -\int_{\Omega_e} \boldsymbol{\nabla}\mathbf{N}\frac{\partial \mathbf{j}}{\partial x_e}^\mathsf{T} \mathrm{d}\Omega_e. \tag{25}$$

We can also reduce the derivatives of the heat and current densities to the element level as

$$\frac{\partial \mathbf{j}}{\partial x_e} = -\frac{\partial \sigma_e}{\partial x_e}\left(\boldsymbol{\nabla}\mathbf{N}^\mathsf{T}\mathbf{V_e} + \alpha_e \boldsymbol{\nabla}\mathbf{N}^\mathsf{T}\mathbf{T_e}\right) + \sigma\frac{\partial \alpha_e}{\partial x_e}\boldsymbol{\nabla}\mathbf{N}^\mathsf{T}\mathbf{T_e},$$

$$\frac{\partial \mathbf{q}}{\partial x_e} = \frac{\partial \alpha_e}{\partial x_e}\left(\mathbf{N}^\mathsf{T}\mathbf{T_e}\right)\mathbf{j} + \alpha_e\left(\mathbf{N}^\mathsf{T}\mathbf{T_e}\right)\frac{\partial \mathbf{j}}{\partial x_e} - \frac{\partial k_e}{\partial x_e}\boldsymbol{\nabla}\mathbf{N}^\mathsf{T}\mathbf{T_e}, \tag{26}$$

where V_e and T_e refer to the nodal values relative to the associated element. To conclude the formulation, we can write the dependence of the material properties on the density variables, [Eq. (12)],

$$\frac{\partial \alpha_e}{\partial x_e} = p_\alpha x_e^{p_\alpha - 1}(\alpha_0 - \alpha_{\min}),$$

$$\frac{\partial k_e}{\partial x_e} = p_k x_e^{p_k - 1}(k_0 - k_{\min}), \tag{27}$$

$$\frac{\partial \sigma_e}{\partial x_e} = p_\sigma x_e^{p_\sigma - 1}(\sigma_0 - \sigma_{\min}),$$

for the SIMP method.

Nevertheless, we still have an extra design variable controlling the voltage across the thermocouple that is not considered in the previous density derivatives, x_e. We store this design variable in the same vector that stores the density design variables with index $n_e + 1$. If we do not apply the boundary conditions to any element with an associated x_e, we can calculate its sensitivity as the matrix product

$$\frac{\mathrm{d}T^*_{avg}}{\mathrm{d}x_{n_e+1}} = +\mathbf{\Lambda}^\mathsf{T}\mathbf{K^k}\frac{\partial \bar{\mathbf{U}}}{\partial V_f}\frac{\mathrm{d}V_f}{\mathrm{d}x_{n_e+1}}, \tag{28}$$

and the derivative of $\mathbf{R}^k$ with respect to the vector of prescribed nodal values $\bar{\mathbf{U}}$ is equal to the rows of the $\mathbf{R}^k$ matrix corresponding to the fixed degrees of freedom in $\bar{\mathbf{U}}$. Now,

the partial derivative of the prescribed degrees of freedom concerning V_f equals one in the prescribed values and zero otherwise. Given the interpolation of the voltage boundary condition, Eq. (14e), its derivative with respect to the $n_e + 1$ design variable is,

$$\frac{\mathrm{d}V_f}{\mathrm{d}x_{n_e+1}} = V_{\max} - V_{\min} \tag{29}$$

which provides all the information needed to calculate the derivative of the objective function.

3.1.2 Volume constraint

For an isotropic material, we calculate the derivative of the volume constraint element-wise using the volume of each element. Starting from the formulation in Eq. (14c), the derivative of the constraint concerning each density variable is,

$$\frac{\mathrm{d}c_v}{\mathrm{d}x_e} = \frac{\partial \sum_{e=1}^{n_e}\left(\frac{x_e v_e}{v_0 v_{obj}}\right)}{\partial x_e} = \frac{v_e}{v_0 v_{obj}}. \tag{30}$$

From this formulation, we can also appreciate that the derivative from any external boundary condition, including voltage, V_f, will be zero,

$$\frac{\mathrm{d}c_{vol}}{\mathrm{d}V_f} = 0. \tag{31}$$

3.1.3 Power constraint

Using the definition of the power consumption in Eq. (15), we can calculate its derivative concerning the density design variable x_e with $e \le n_e$,

$$\frac{\mathrm{d}P_e}{\mathrm{d}x_e} = -\int_\Omega \left(\frac{\mathrm{d}\mathbf{j}}{\mathrm{d}x_e}\right)^\mathsf{T}\boldsymbol{\nabla}\mathbf{N}^\mathsf{T}\mathbf{V_e}\,\mathrm{d}\Omega - \int_\Omega \mathbf{j}^\mathsf{T}\boldsymbol{\nabla}\mathbf{N}^\mathsf{T}\frac{\mathrm{d}\mathbf{V_e}}{\mathrm{d}x_e}\,\mathrm{d}\Omega. \tag{32}$$

The current density in the previous equation depends on the nodal voltages and temperature values given by Eq. (2). The derivative of the current density can be written as,

$$\frac{\mathrm{d}\mathbf{j}}{\mathrm{d}x_e} = -\frac{\partial \sigma}{\partial x_e}\left(\boldsymbol{\nabla}\mathbf{N}^\mathsf{T}\mathbf{V_e} + \alpha\boldsymbol{\nabla}\mathbf{N}^\mathsf{T}\mathbf{T_e}\right)$$
$$- \sigma\left(\boldsymbol{\nabla}\mathbf{N}^\mathsf{T}\frac{\mathrm{d}\mathbf{V_e}}{\mathrm{d}x_e} + \frac{\partial \alpha}{\partial x_e}\boldsymbol{\nabla}\mathbf{N}^\mathsf{T}\mathbf{T_e} + \alpha\boldsymbol{\nabla}\mathbf{N}^\mathsf{T}\frac{\mathrm{d}\mathbf{T_e}}{\mathrm{d}x_e}\right). \tag{33}$$

In this equation, we can separate the components that multiply the derivatives of the system nodal degrees of freedom, $\mathbf{L_{dUe}}$, from the rest of the integrator, L_{Ue}, element-wise,

$$L_{Ue} = \mathbf{V_e}^\intercal \boldsymbol{\nabla N} \frac{\partial \sigma}{\partial x_e} \boldsymbol{\nabla N}^\intercal \mathbf{V_e}$$
$$+ \mathbf{V_e}^\intercal \boldsymbol{\nabla N} \left(\frac{\partial \alpha}{\partial x_e} \sigma + \alpha \frac{\partial \sigma}{\partial x_e} \right) \boldsymbol{\nabla N}^\intercal \mathbf{T_e}, \tag{34}$$
$$\mathbf{L_{dUe}} = \begin{bmatrix} \mathbf{V_e}^\intercal \boldsymbol{\nabla N} \sigma \alpha \boldsymbol{\nabla N}^\intercal \\ \mathbf{V_e}^\intercal \boldsymbol{\nabla N} \sigma \boldsymbol{\nabla N}^\intercal - \mathbf{j}^\intercal \boldsymbol{\nabla N}^\intercal \end{bmatrix},$$

We can observe that the first term L_{Ue} is a constant value within the element, and we can extract this term outside the integral,

$$\frac{dP_e}{dx_e} = L_{Ue} v_e + \int_\Omega \left(\mathbf{L_{dUe}}^\intercal \frac{d\mathbf{U_e}}{dx_e} \right) d\Omega. \tag{35}$$

Applying the summation from Eqs. (15) and (35) we can assemble both terms, L_{Ue} and $\mathbf{L_{dUe}}$, for the full system nodal values into $\mathbf{L_U}$ and $\mathbf{L_{dU}}$, respectively. The result taking the derivative for all density values, x_e with $e \leq n_e$ is,

$$\frac{dP}{dx} = \mathbf{L_U} + \mathbf{L_{dU}}^\intercal \frac{d\mathbf{U}}{dx}, \tag{36}$$
$$\mathbf{L_U} = \begin{bmatrix} L_{U1} v_1 & L_{U2} v_2 & \cdots & L_{UN} v_N \end{bmatrix},$$

Introducing the derivative of the power, Eq. (36), in the constraint derived in Eq. (14d) and using an equivalent formulation with an adjoint vector, $\boldsymbol{\Lambda_P}$, multiplied by the residuals we obtain,

$$c_{pow}^* = \frac{P}{P_{obj}} - 1 + \boldsymbol{\Lambda_P}^\intercal \mathbf{R}^k, \tag{37}$$

The derivative of this new c_{pow}^* can be re-written as,

$$\frac{dc_{pow}^*}{dx} = \frac{\frac{dP}{dx}}{P_{obj}} + \boldsymbol{\Lambda_P}^\intercal \frac{d\mathbf{R}^k}{dx}, \tag{38}$$

where we can substitute Eq. (36),

$$\frac{dc_{pow}^*}{dx} = \frac{1}{P_{obj}} \left(\mathbf{L_U} + \mathbf{L_{dU}}^\intercal \frac{d\mathbf{U}}{dx} \right)$$
$$+ \boldsymbol{\Lambda_P}^\intercal \left(\frac{\partial \mathbf{R}^k}{\partial x} + \mathbf{K}^k \frac{d\mathbf{U}}{dx} + \frac{\partial \mathbf{R}^k}{\partial \bar{\mathbf{U}}} \frac{\partial \bar{\mathbf{U}}}{\partial V_f} \frac{dV_f}{dx} \right) \tag{39}$$

Finally, we can select the adjoint vector $\boldsymbol{\Lambda_P}$ imposing that the components of the derivative of the system nodal degrees of freedom, $\frac{d\mathbf{U}}{dx}$, are removed from the equation as,

$$\boldsymbol{\Lambda_P} = -(\mathbf{K^k})^{-\intercal} \left(\frac{1}{P_{obj}} \mathbf{L_{dU}} \right). \tag{40}$$

Equation (40) can now be used with Eq. (39) to calculate the derivatives concerning the density variables, reducing it to the element level as,

$$\frac{dc_{pow}^*}{dx_e} = \frac{1}{P_{obj}} L_{Ue} \mathbf{V_e} + \boldsymbol{\Lambda_{Pe}}^\intercal \frac{\partial \mathbf{R}^k}{\partial x_e}, \tag{41}$$

where Eq. (25) provides the derivative of the residual concerning the element density.

The calculation of the derivative concerning the x_{n_e+1} design variable controlling the voltage gradient across the thermocouple, Eq. (14e), can be calculated by noticing that the material properties do not depend on the voltage $(\alpha, \sigma, k \neq f(V_f))$, $L_{Ue} = 0$. We can calculate the derivative as

$$\frac{dc_{pow}^*}{dx_{n+1}} = +\boldsymbol{\Lambda_P}^\intercal \frac{\partial \mathbf{R}^k}{\partial \bar{\mathbf{U}}} \frac{\partial \bar{\mathbf{U}}}{\partial V_f} \frac{dV_f}{dx_{n+1}}. \tag{42}$$

where the conclusion and procedure from Eq. (28) can still be applied with the new adjoint vector, $\boldsymbol{\Lambda_P}$.

4 Results

SIMP shows excellent results in mechanical problems with penalty factors, p_i, higher than 1 and usually equal to 3. However, for high nonlinear or "multi-physics" problems, these coefficients might need to be re-evaluated empirically to improve the convergence of TO (?).

In this section, we study the use of an analytical problem of low dimension that can help to provide insight into the larger FEM problem. Notably, we want to understand the influence of the parameters introduced in the optimization—material penalty coefficients—and the starting points of the MMA algorithm over the optimized designs.

Finally, the proposed method in Sect. 4.2 is applied to a FEM thermocouple model using the insight obtained from the analytical model and with the application of different heat extraction and power consumption requirements, studying their effects over the optimized designs.

4.1 Landscape study through analytical models

For a thermocouple optimization, a parallel semiconductor problem with two pillars per thermoelectric leg and two design variables, x_1 and x_2—associated with each one of the two pillars of each thermoelectric leg, see Fig. 2—provides one of the smallest problems that we can solve analytically, providing insights into the problem and avoiding electrical and thermal disconnections.

The schematic in Fig. 2 describes a problem with two legs for each pellet with two different density variables, x_1 and x_2, in each electrical connection to the copper layers—elements shaded in gray—to avoid disconnected designs unless both density variables are equal to zero. The heat injection, q_{in}, ground voltage level, V_0, with the voltage
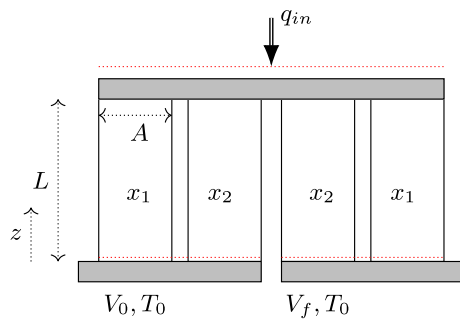
Fig. 2 Thermocouple analytical problem schematic with four columns and two density design variables, x_1 and x_2. We define the geometry of the design through a constant cross-section area A and height L, with the height dimension represented by the z coordinate. The boundary conditions are represented by a heat injection q_{in}, a heat sink temperature T_0 and two voltages, V_0 and V_f

gradient V_f and constant temperature sink T_0 represent the boundary conditions for the problem. Finally, A and L provide each column's cross-sectional area and height, with z representing a certain height along the legs starting from the heat sink.

Notice that we apply the boundary conditions at the bottom and top of each leg or semiconductor column in the copper layers connections, providing the compatibility equations between the legs, which we can write using Eqs. (1)–(3) and Fig. 2 as

$$
\begin{aligned}
&\sum_{xi} q_{p,xi}(L) + \sum_{xi} q_{n,xi}(L) = -\frac{q_{in}}{A}, \\
&\sum_{xi} j_{p,xi}(L) + \sum_{xi} j_{n,xi}(L) = 0, \\
&T_{p,xi}(L) = T_{n,xi}(L) = T_c, \\
&\phi_{p,xi}(L) = \phi_{n,xi}(L) = V_c, \\
&T_{p,xi}(0) = T_{n,xi}(0) = T_0, \\
&\phi_{p,xi}(0) = V_0 = 0, \\
&\phi_{n,xi}(0) = V_f,
\end{aligned}
\tag{43}
$$

where p and n indices refer to the p or n-type semiconductors—positioned in series through a copper connection—and xi to the design variable associated with each parallel leg, Fig. 2. Finally, T_c and V_c represent the unknown values in the top cold connection at location $z == L$ according to Fig. 2.

The solution of the integration of Eqs. (1)–(3) along the length, z, of a constant cross-section leg provides,

$$
\begin{aligned}
T(z) &= -\frac{j^2}{k\sigma}\frac{z^2}{2} + C_1 z + C_2, \\
\phi(z) &= +\frac{\alpha j}{\sigma k}\frac{z^2}{2} - \frac{j}{\sigma}z + \alpha C_3 z + C_4,
\end{aligned}
\tag{44}
$$

where the C_i are constants that need to be solved using the boundary conditions Eq. (43). The voltage and temperature distributions of Eq. (44) are quadratic functions across the bulk material with constant material coefficients.

The semiconductor material properties for each of the $p - \mathrm{Bi_2Te_3}$ and $n - \mathrm{Bi_2Te_3}$ pellets are available from the manufacturer and taken from Hu et al. (2015) where the data from ULVAC-Riko Co. Ltd is fit to polynomials of the form,

$$
\begin{aligned}
\alpha_p &= 8.33e{-}12T^3 - 1.32e{-}8T^2 + 6.3e{-}6T - 7.04e{-}4, \\
\rho_p &= -7.36e{-}13T^3 + 6.14e{-}10T^2 - 6.35e{-}8T - 1.78e{-}6, \\
k_p &= 1.59e{-}8T^3 - 3.32e{-}6T^2 - 2.177e{-}3T + 1.5775, \\
\alpha_n &= -3.98e{-}12T^3 + 7.34e{-}9T^2 - 3.82e{-}6T + 3.95e{-}4, \\
\rho_n &= -6.83e{-}13T^3 + 6.66e{-}10T^2 - 1.55e{-}7T + 1.81e{-}5, \\
k_n &= 2.19e{-}8T^3 - 4.60e{-}6T^2 - 4.51e{-}3T + 2.48,
\end{aligned}
\tag{45}
$$

where each subindex refers to p-type or n-type semiconductors, respectively. We ignore the copper Seebeck coefficient due to symmetry, with its effects counteracted in the full thermoelectric circuit. To simplify the problem to constant material properties, we fix the values at 300 K as summarized in Table 1.

To solve the system, we require the C_i constants for four different legs leading to a system of 11 equations, plus an additional equation for the power,

$$
P = -A\left(\sum j_{li}(V_c - V_0) + \sum j_{ri}(V_f - V_c)\right)
\tag{46}
$$

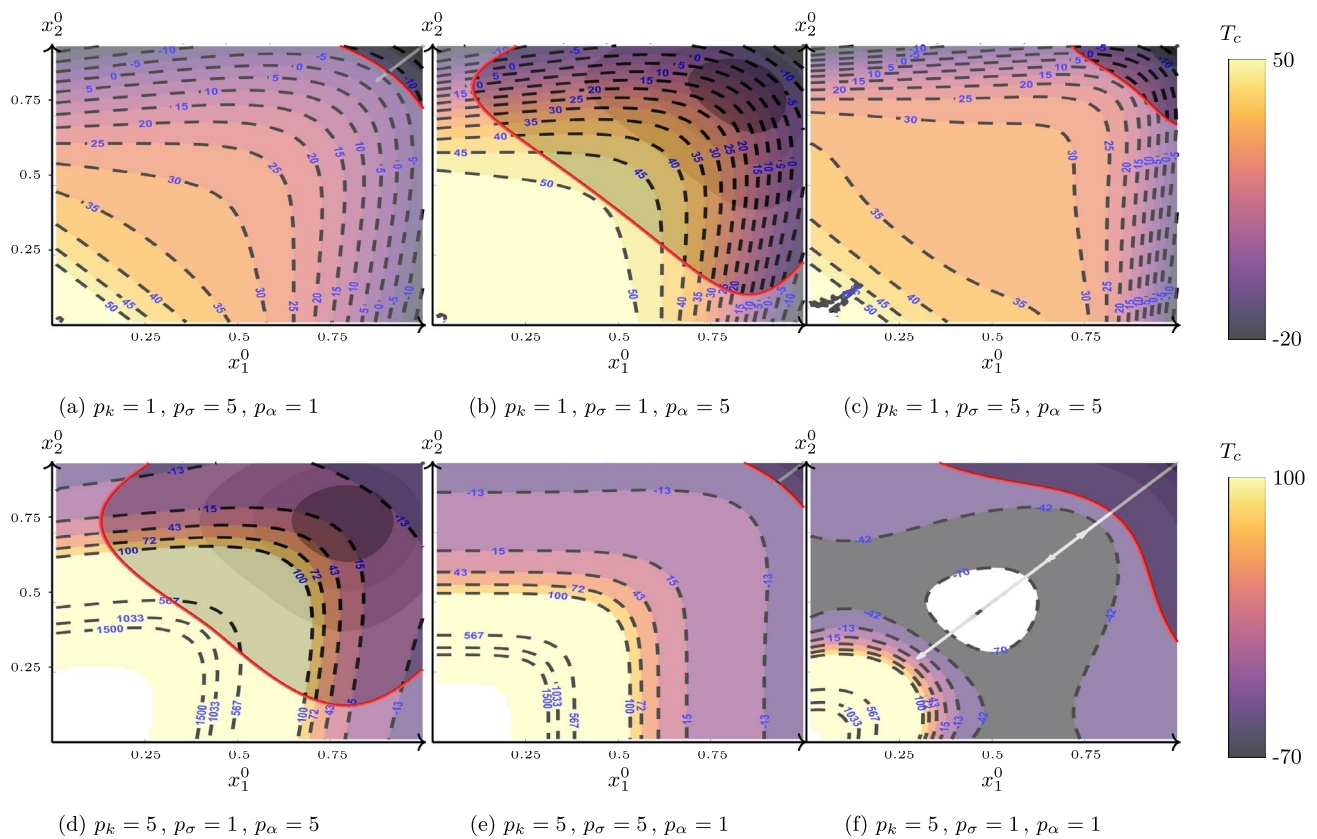for constant values of the material coefficients (α, σ, k).

To solve the system, we select a given operational point, defined by all the parameters needed to solve the problem, given by,

$$
\begin{aligned}
&T_0 = 298.15\,\mathrm{K}, \quad q_{in} = 0.01\,\mathrm{W\,m^{-2}}, \\
&L = 1.2\,\mathrm{mm}, \quad A = 1\,\mathrm{mm^2}, \quad V_f = 0.05\,\mathrm{V},
\end{aligned}
$$

and the parametric solution to Eqs. (43) and (44) found in Sect. B. Notice that in this solution, we set all minimum material properties—α_{min}, k_{min} and σ_{min} from Eq. (12)—to zero for simplification purposes.

The quadratic nature of the system provides two different solutions. We look for a solution with temperatures above absolute zero to evaluate which one has a physical meaning. For the material properties, we use the values of the p-semiconductor from Table 1. Notice that, to account for an n-type semiconductor using a given direction of the current and a constant positive α, we need to provide a negative sign to the Seebeck coefficients using Eq. (44).

In Fig. 3, we represent the objective temperature, T_c, for multiple combinations of the material penalty coefficients.

(a) $p_k = 1$, $p_\sigma = 5$, $p_\alpha = 1$

(b) $p_k = 1$, $p_\sigma = 1$, $p_\alpha = 5$

(c) $p_k = 1$, $p_\sigma = 5$, $p_\alpha = 5$

(d) $p_k = 5$, $p_\sigma = 1$, $p_\alpha = 5$

(e) $p_k = 5$, $p_\sigma = 5$, $p_\alpha = 1$
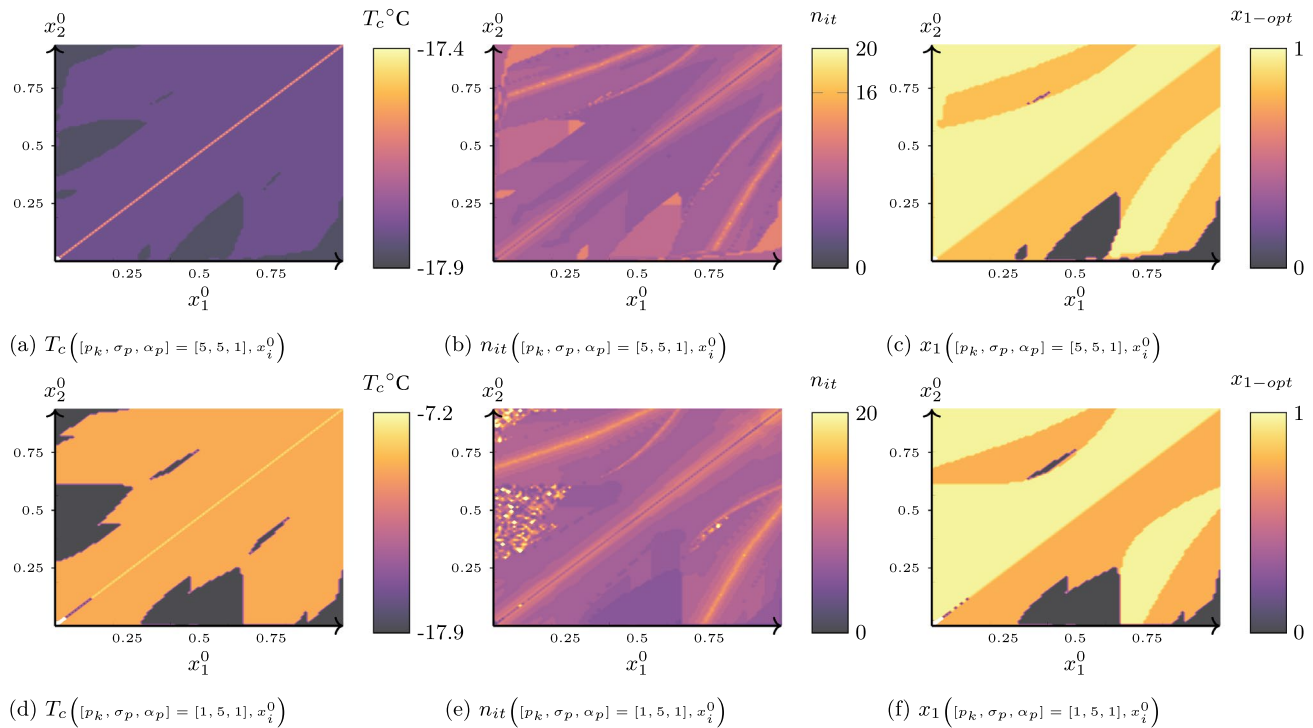
(f) $p_k = 5$, $p_\sigma = 1$, $p_\alpha = 1$

Fig. 3 Material penalization coefficient cold temperature isolines for a 4-column TEC problem with two design variables and a power constraint, shadowed in black. The MMA optimization starting with the point (1, 1) is reflected with gray to black lines turning darker until convergence

The unfeasible region of the power constraint, given by Eq. (46), is superposed to T_c as a gray-shadowed region limited by a red line. We represent this power consumption with a darker gray color the higher the power consumption to visualize its landscape. The path followed by the MMA optimizer, drawn with gray arrows that grow darker with successive iterations, starting from a full-density design—$x_i = 1$ for both design variables—provides information on the convergence of the problem.

We find 3 different possible landscapes depending on the material penalty coefficients, which will affect the convergence of the problem. Except for Fig. 3f, all penalty coefficients present an objective temperature global minima in the full-density design point, and local minima at the locations with one single design variable with full density, i.e., $x_1 = 0$ and $x_2 = 1$ or $x_1 = 1$ and $x_2 = 0$. With regards to the power constraint, it can either present a negative slope in all the unfeasible design regions (Figs. 3a, e, f) or set the full-density design point in a valley region, having a maximum within the non-feasible region (Figs. 3b, d).

These landscapes affect the convergence of MMA. The landscapes where the power presents a maximum in the unfeasible design space do not move from the initial point, chosen as the full-density design, as all directions increase the constraint value. This non-convexity leads to results within the non-feasible design space in the cases in Figs. 3b, d. From the remaining cases, we want to avoid global minima in gray design areas that lead to equivalent non-manufacturable porous materials, such as Fig. 3f.

To further identify the best combination of penalty coefficients for this problem, we look into the convergence properties and final results of Fig. 3a, e, which show convergence from the full-density design to local minima in the feasible design space. Between both cases, Fig. 3e shows a steeper design space and lower achieved objective values. However, different initial design points might influence these results. Figure 4 studies these two cases for multiple initial points, x_i^0, represented on the horizontal and vertical axis, and plotting in color the final temperature values, number of iterations until convergence, n_{it}, and x_{1-opt} or optimal x_1 design variable. We do not represent the design variable x_{2-opt} due to the symmetry of the problem.

(a) $T_c \left([p_k, \sigma_p, \alpha_p] = [5, 5, 1], x_i^0 \right)$

(b) $n_{it} \left([p_k, \sigma_p, \alpha_p] = [5, 5, 1], x_i^0 \right)$

(c) $x_1 \left([p_k, \sigma_p, \alpha_p] = [5, 5, 1], x_i^0 \right)$

(d) $T_c \left([p_k, \sigma_p, \alpha_p] = [1, 5, 1], x_i^0 \right)$

(e) $n_{it} \left([p_k, \sigma_p, \alpha_p] = [1, 5, 1], x_i^0 \right)$

(f) $x_1 \left([p_k, \sigma_p, \alpha_p] = [1, 5, 1], x_i^0 \right)$

Fig. 4 Graphs exemplifying the final convergence values of a cold temperature T_c MMA optimization of a 2D analytical thermocouple with a power constraint of 0.065 W for different initial design variables in the horizontal and vertical axis. The top figures represent the results of T_c, total iterations until convergence and the optimal x_1 found (x_{1-opt}) for a combination of penalty coefficients of $p_k = p_\sigma = 5, p_\alpha = 1$ while the bottom row uses the penalty coefficients $p_k = p_\alpha = 1, p_\sigma = 5$

Table 1 TEC semiconductor material properties at 300 K

	ρ (Ω m)	k (W K^{-1})	α (v K^{-1})
$p - \mathrm{Bi_2Te_3}$	1.45e-05	1.054963	2.17e-04
$n - \mathrm{Bi_2Te_3}$	1.30e-05	1.305023	−1.99e-4
Cu	1.67e-08	385	0

Figure 4a, d shows that both penalty coefficients can reach similar values for T_c depending on the initial chosen point. However, the case $p_k = 5, p_\sigma = 5, \alpha = 1$ shows a lower dispersion in the results from different initial points. There is no better configuration regarding the number of iterations until convergence. Still, it does suggest that values slightly off the full-density design might reduce the number of iterations until convergence. Both combinations of penalty coefficients show numerical errors at low initial density values for both design variables due to the disconnection between the boundary conditions, which leads to values close to infinity in T_c.

The previous study only considered the power constraint. We now introduce the volume constraint through the definitions in Eq. (30) to study the entire landscape. The new landscape in Fig. 5 uses a power constraint of
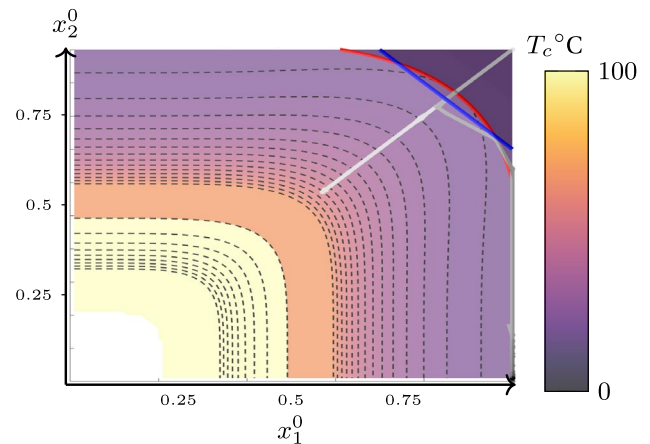
Fig. 5 Temperature landscape for a 2D analytical thermocouple optimization with a power constraint of 0.05 W and 85 % initial volume with the non-allowed design space shadowed in gray

0.05 W in addition to a volume constraint of 85 %. This volume constraint appears as a straight line at 135 °, and its location gives rise to 3 distinct cases depending on the constraint limit. We can find that both constraints, volume and power, cross each other Fig. 5, with the possibility of
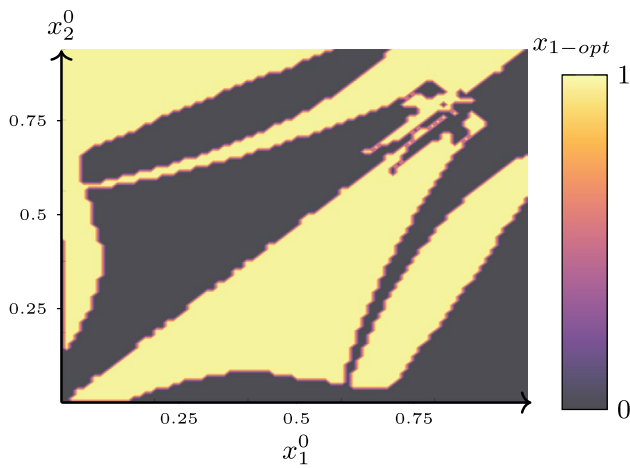
Fig. 6 Design variable, x_{1-opt}, of the obtained local minima in the analytical problem for 85 MMA iterations of a 2D analytical thermocouple optimization with a power constraint of 0.05 W and 85 % initial volume

either of them being active at convergence or finding one of them being the most limiting, in which case it will be the only constraint to be active at convergence.

Figure 6 represents the value for the optimal x_1 design variable found, x_{1-opt}, for a maximum of 85 iterations with respect the initial design variables, x_1^0 and x_2^0, represented in the horizontal and vertical axis using the previously defined problem, with power and volume constraints. Compared to Fig. 4, this graph shows that the algorithm removes intermediate-density values from the converged results, and only 2 solutions remain. These remaining solutions are the local minima with one of both design variables equal to one and the other one equal to zero.
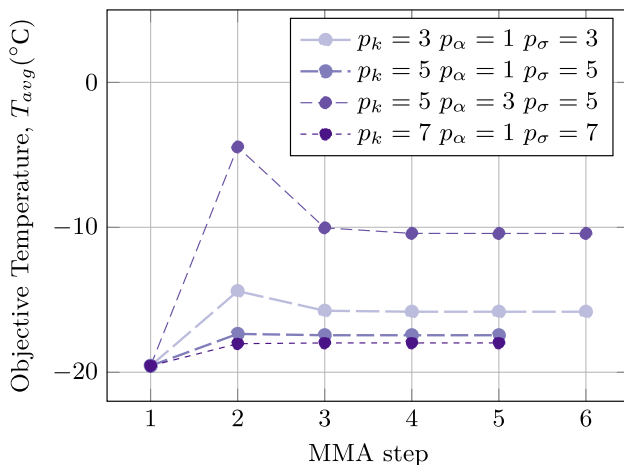
Fig. 7 Convergence of the objective function for several penalty coefficients in a thermocouple analytical model

As a last consideration, Fig. 7 shows the convergence of the objective function for different penalty values for the case $p_\alpha < p_\sigma = p_k$ starting from a full-density design. While higher values of $p_k = p_\sigma$ provide lower objective values, the higher these values, the higher the nonlinearities introduced in the problem. The case with a nonlinear penalty coefficient for p_α shows worse convergence and final results and should be avoided.

Notice that Figs. 3b–c cases did not converge starting from a full-density design. However, these study cases might converge from different initial design locations. Nevertheless, lacking information on the optimized design, a homogeneous density equal to the full density as a starting point is desirable for larger problems.

The results and reasoning in this section lead to the recommendation of penalty coefficients of $p_k = p_\sigma > p_\alpha = 1$ and initial density values of $x_e = 1$.

## 4.2 Thermocouple optimization examples through FEM

This section showcases optimization examples using the proposed TO methodology based on the 1MC10-031 TEC from RMT Ltd. The data sheet of the 1MC10-031 TEC provides the dimensions of $1.2 \times 1 \times 1$ mm^3 separated by an air-gap of 0.4 mm which we reduce in 0.1 mm to have a larger feasible semiconductor design volume.

In this model, we assume a uniformly distributed heat input along the top surface of the thermocouple. We also model the heat sink as having a constant temperature at its bottom. We consider the TEC to consist of 32 pairs of pellets, N_p, considered for the calculation of the boundary conditions as,

$$q_{in} = q_T/N_p,$$
$$P_c = P_T/N_p,$$

where P_T and P_c represent the TEC's total heat extraction and power consumption, assuming each pair extracts equal heat. Additionally, a voltage gradient is imposed between
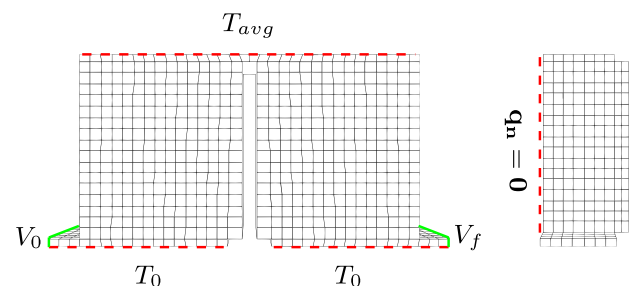

Fig. 8 Front and side view of the thermocouple mesh with the applied boundary and symmetry conditions

both copper slabs, with a value of 0 close to the p-type semiconductor and the desired electrical potential, V_f, at the other electrical contact, see Fig. 8. This $V_f = 0.05$ V is modified through the design variable x_{n_e+1} with limits between $0.5V_f$ and $2V_f$, equivalent to V_{min} and V_{max} in Eq. (14e).

We represent the mesh and boundary conditions in Fig. 8 where we use symmetry boundary conditions, simplifying the thermocouple model and imposing no heat or current fluxes through this surface. The copper is a non-design domain used to apply the surface boundary conditions. We should consider additional terms to the previously calculated sensitivities if the copper is within the design domain.

We can now run the FEM optimization with multiple boundary conditions and constraints using the material properties specified in Table 1. To avoid numerical singularities, following Eq. (12), all material properties have a minimum scaling value of 1e-9. To compare to the analytical model, we first select a constant value of 5333 W m^{-2} as heat injection and 0.011 W as power constraint with different penalty coefficients.

In the previous Sect. 4.1, we predict the behavior of the thermoelectrical optimization problem for multiple penalization coefficients. In particular, the combination $p_k = p_\sigma > p_\alpha$ shows the most promise, while the rest of the combinations lead to higher minima values and non-feasible results. If we repeat this study with the unsatisfactory penalty coefficients using the FEM problem, we obtain Fig. 9. In this figure, we observe the convergence of the objective value and constraints using the rejected penalization coefficients. In all these cases, we observe that, while there is no volume constraint—it is set to 100% of the original volume—most optimizations get stuck at full volume. We can correlate this issue to the cases studied in analytical form, where we find a maximum value in the power constraint close to the full volume, which makes it difficult to achieve convergence in MMA. Furthermore, we can also appreciate that the combination $p_k > p_\sigma = p_\alpha$ leads to a disconnection of the electrical circuit, leading to heating of the objective surface and an eventual non-convergence of the Newton–Raphson FEM solver. The prediction from the analytical model also leads
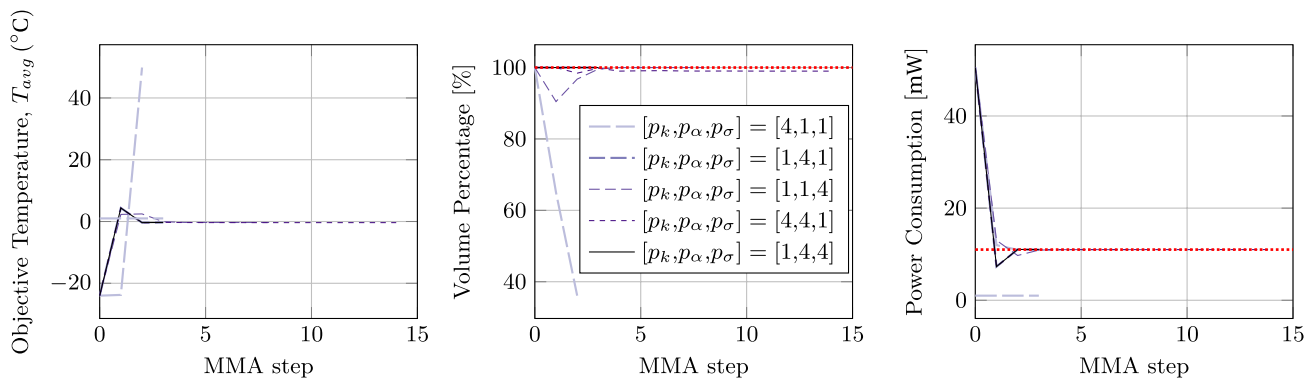
Fig. 9 Convergence of the objective and constraint functions—constrained limit in red—for discarded penalization coefficients combinations following the development in Sect. 4.1, starting with a full-density design
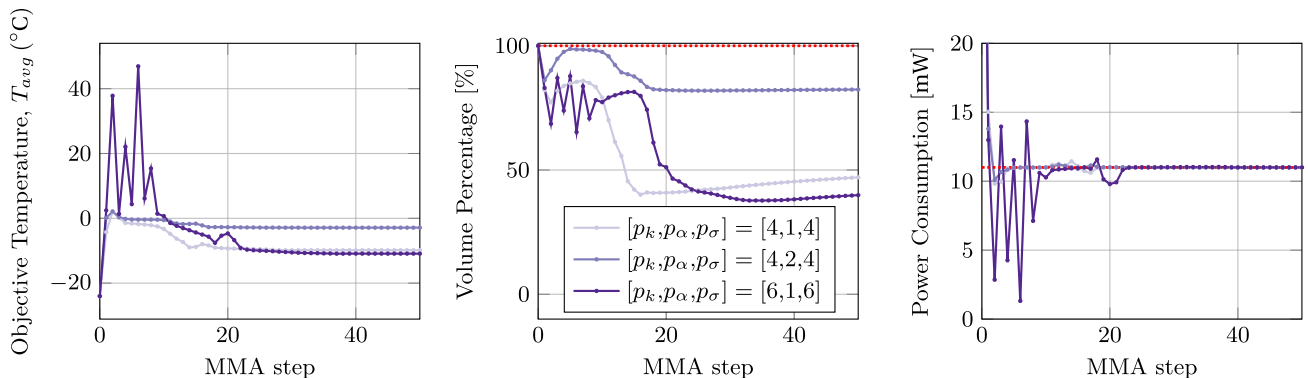

Fig. 10 Convergence of the objective and constraint functions—constrained limit in red—for three combinations of penalization coefficients following the approach that showed good convergence in Sect. 4.1, $p_k = p_\sigma > p_\alpha$, starting with a full-density design

us to think that the combination $p_k = p_\sigma > p_\alpha$ can remove the convergence issues found with the other combinations.

Figure 10 shows the convergence history of three different configurations of penalty coefficients with the objective and constraint values using the penalization coefficient format, $p_k = p_\sigma > p_\alpha$. Furthermore, the limiting values in both constraint plots, v_{obj} and P_{obj}, are drawn as red dotted lines. In Fig. 10, we observe from the temperature objective path that higher penalty factors with a linear p_α lead to large oscillations until the algorithm provides a solution close to the minima. Furthermore, the model with higher order p_α demonstrated a smoother convergence, but the final result was 8 °C higher compared to the linear penalty coefficient case. Finally, the increased $p_\alpha = p_k = 6$ model only achieved a 1 °C improvement compared to $p_\alpha = p_k = 4$. These results imply that larger coefficients can lead to improved designs, but the gains might not compensate for the convergence deterioration. Nevertheless, all combinations of penalty coefficients using $p_k = p_\sigma > p_\alpha$ converge to optimal values volumes with lower minima than all other tested combinations as predicted in Sect. 4.1.

Looking at the constraint convergence results, we further observe that while the power constraint always becomes active—the TEC uses all available power—the volume constraint does not always remain active, with a total volume under the imposed v_{obj}. Furthermore, the volume continues to increase after the convergence of the objective temperature value, which remains constant with less than 0.001 °C variation from the 20th iteration. This increase in volume after the objective convergence introduces low intermediate-density values electrically disconnected to the rest of the system and, as such, are not relevant for the final manufacturable design and are visualized in the resulting design in Fig. 11.
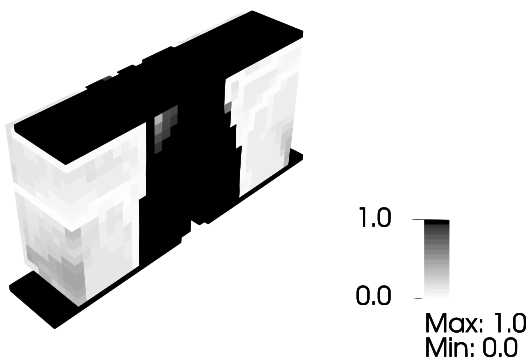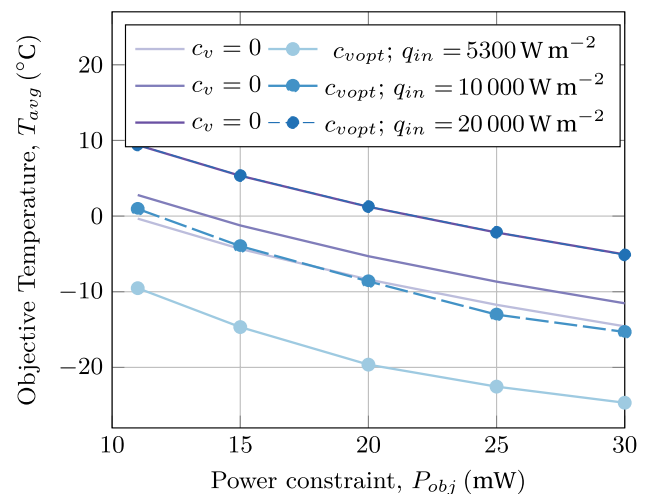
Figure 11 shows the result of an optimization where each element is colored from white to black depending on its associated density. We can appreciate that we obtained column-like structures with surrounding gray or intermediate-density regions in this plot. These gray regions are disconnected from the rest of the design, with densities under 2 %. However, these gray elements do not transmit heat or electrical current as we do not appreciate any effect over the objective function.

Maintaining a constant value for the penalty coefficient of $p_k = p_\sigma = 4$ and $p_\alpha = 1$, we can run the optimization for different heat injection, power, and volume constraint values to understand the effect of the boundary conditions and constraints on the final converged designs.

Figure 12 shows the effect, over the objective value, of the change in the heat injection and power constraint in successive blue lines. Furthermore, since we use the voltage as a design variable, we can compare it with the lowest temperature value achievable in the full-density design for the same power consumption, seen as purple lines in the same plot. The different curves show that a higher power constraint provides lower temperature values. However, there seems to be an asymptotic behavior with smaller gains for higher power constraint values. Furthermore, an increase in heat injection results in a vertical translation of the objective function toward higher temperature values, with smaller gains with respect to the initial design. This effect can be taken to the limit, where the optimal solution results in the full volume design at high enough heat injections. The overlap in the purple and blue lines in Fig. 12 confirms this statement.

Fig. 11 Element density, x_e, for a converged thermocouple TO with for boundary conditions and constraints $q_{in} = 5333 \, \mathrm{W^2 m^{-1}}, P_{obj} = 11 \, \mathrm{mW}$ and $v_{obj} = 0.3$

Fig. 12 Change in the final average temperature T_{avg} with respect to the heat injection and power constraint. The figure compares the lowest temperature achievable for each power in the full-density design, $c_v = 0$, to the optimal designs, c_{vopt}. We provide the results for multiple heat injections, detailed in the figure legend
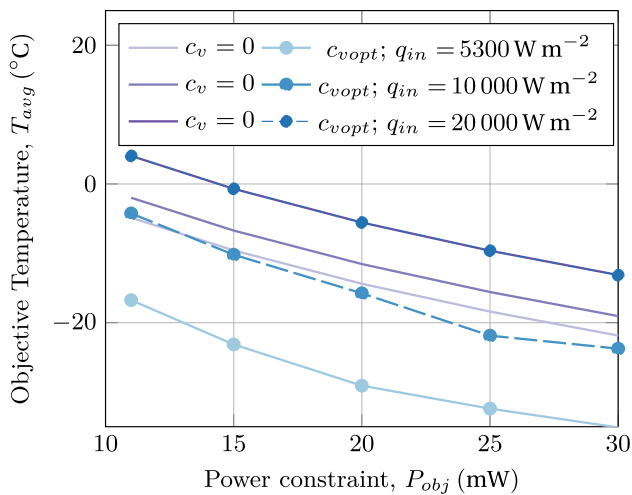
Fig. 13 Postprocessing of the optimal designs in Fig. 12 using a full nonlinear material formulation following Eq. (45) plotted in blue. In violet, we compare the optimal results to the full-density designs, $c_v = 0$, using nonlinear material properties in both cases
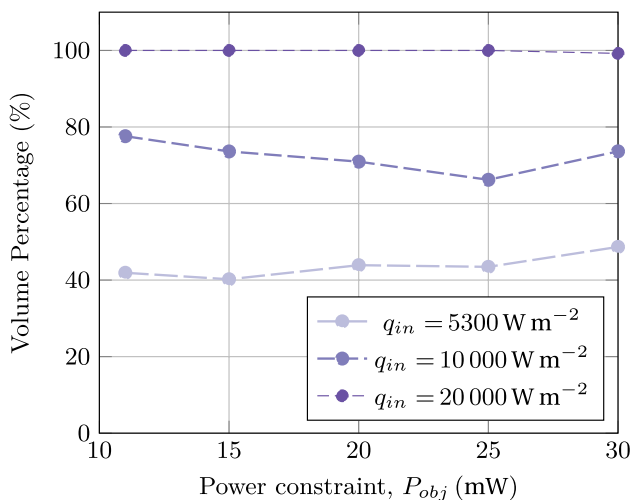
Fig. 14 Change in the final design volume percentage over the total initial volume concerning the heat injection and power constraint

As we obtain the optimization results using constant material properties with temperature, it is convenient to post-process them using a nonlinear material property formulation following PérezAparicio et al. (2007). The results plotted in Fig. 13 show the optimal designs found with constant material properties, run using the material properties in Eq. (45). This plot shows the full-density results for nonlinear material properties in purple for comparison purposes. These results show that, while the results differ from the constant material properties, in all cases, the optimal still performs better than the original design at a lower computational cost and lower non-convexities.

We can also appreciate the effect of the loading conditions over the optimal thermocouple volume. Figure 14 shows the final volume of the designs against the power constraint and heat injection values, calculated as,

$$v_\% = \frac{\sum_e^{n_{x>0.9}} x_e}{v_0}, \tag{47}$$

where $n_{x>0.9}$ denotes only the elements with densities higher than 0.9, to account for the resulting intermediate-density elements. The higher the heat injection in Fig. 14, the higher the amount of semiconductor volume for the optimized geometry of the thermocouple. Indeed, at the highest studied heat injection values, the optimizer does not move from the initial full-density design. The optimizer can converge at lower thermocouple volumes for lower heat injection values, achieving a minimum objective value at a given power constraint.

While in the previous studied scenarios, the volume constraint was set to full volume and always satisfied, activating the constraint to limit the amount of semiconductor material and reduce material costs is interesting. Figure 15 shows in blue lines the effect of lower volume constraints for the largest heat input studied of $20000\,\mathrm{W\,m^{-2}}$—whose converged design is always at full density—and increased power constraints relative to the obtained optimized temperature. This plot shows that for small volume reductions, there are small decreases in the objective function value, which is evidence that the design space is flat in this region of the landscape. However, Fig. 15 presents a critical value of the volume constraint—around 70% volume—where the objective value
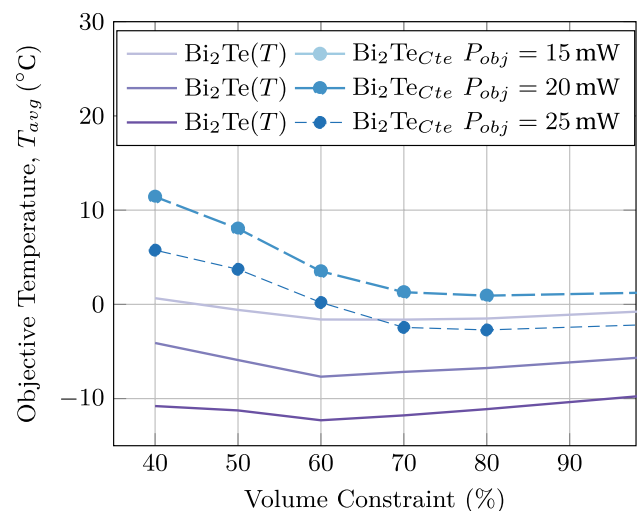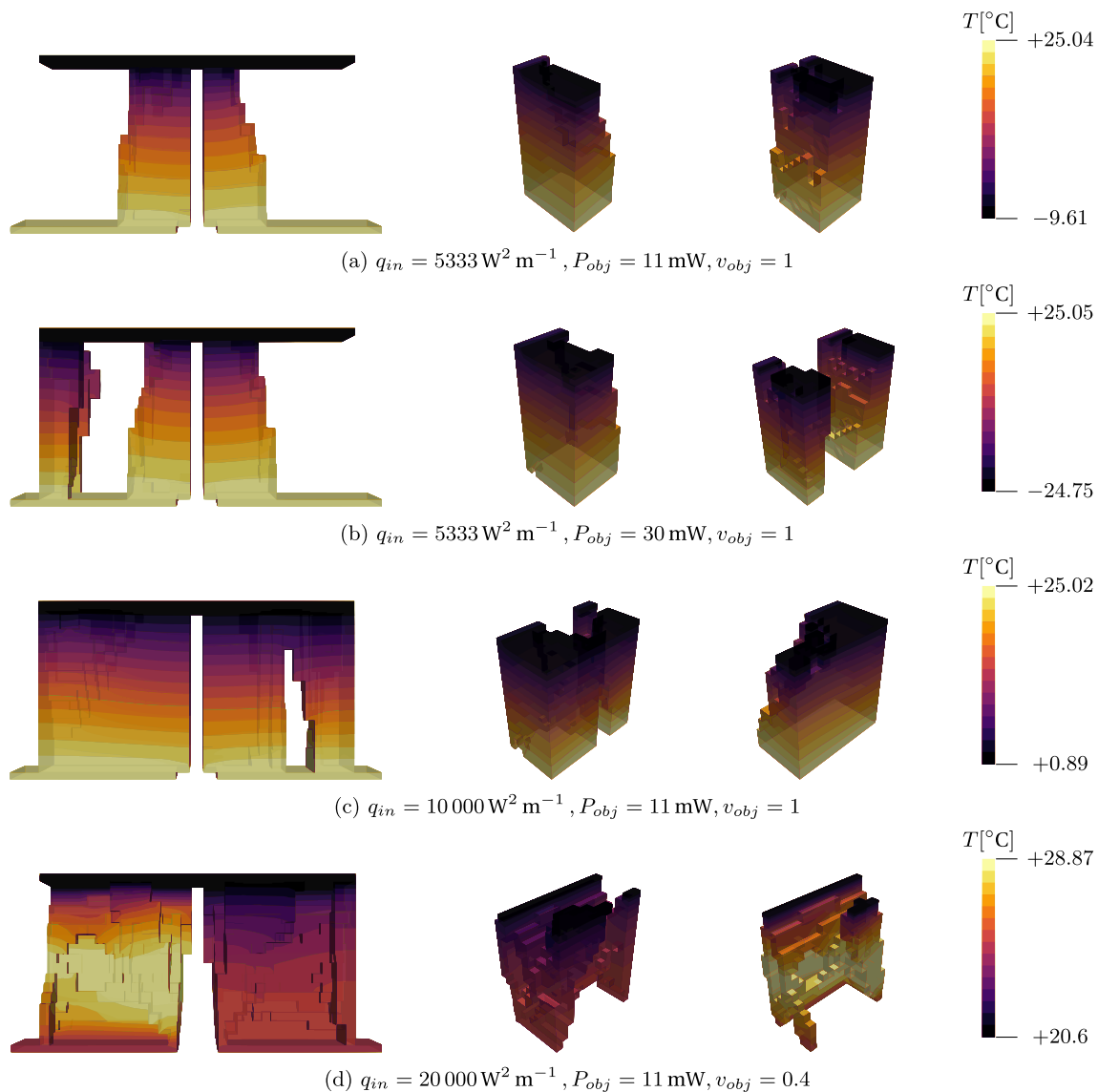

Fig. 15 Change in the final average temperature, T_{avg}, with respect to the volume constraint v_{obj} and the power constraint, P_{obj} for a constant heat injection. The results plotted include the temperature-dependent postprocessing of the optimizations following Eq. (45) in purple

increases rapidly. This behavior is still present if we post-process the results with nonlinear material properties Eq. (45), plotted as purple lines in Fig. 15. However, nonlinear material properties slightly decrease the objective function for lower volumes, in the order of 2 degrees, compared to the full volume design optimum. This result means that while the optimizations performed with constant material properties provide better designs with lower computational nonlinearities, the problem can present better minima running with nonlinear material properties.

All these simulations use an averaged temperature objective, taking as a hypothesis that there are no hot spots on the cold surface. In all the resulting optimal designs, the change

in the temperature distribution in the thermocouple cold side surface is lower than 0.2 °C. These results remain valid after postprocessing the optimal results using nonlinear material properties. This temperature change along the objective surface is small enough to accept the initial hypothesis taken, stating that the temperature of this surface is homogeneous. If this difference were larger, an aggregation function rather than the average temperature of the surface would need to be incorporated to take into account the higher sensitivity of the hot spots.

Once we understand the effect of the different parameters on the optimization, we can look into the resulting designs. Figure 16 shows the geometry and temperature field of the

(a) $q_{in} = 5333\,\mathrm{W}^2\,\mathrm{m}^{-1}$, $P_{obj} = 11\,\mathrm{mW}$, $v_{obj} = 1$

(b) $q_{in} = 5333\,\mathrm{W}^2\,\mathrm{m}^{-1}$, $P_{obj} = 30\,\mathrm{mW}$, $v_{obj} = 1$

(c) $q_{in} = 10\,000\,\mathrm{W}^2\,\mathrm{m}^{-1}$, $P_{obj} = 11\,\mathrm{mW}$, $v_{obj} = 1$

(d) $q_{in} = 20\,000\,\mathrm{W}^2\,\mathrm{m}^{-1}$, $P_{obj} = 11\,\mathrm{mW}$, $v_{obj} = 0.4$

Fig. 16 Elements with densities $x_e > 0.99$ resulting from TO of a thermocouple following Sect. 4.2 for several boundary conditions and constraints. The temperature plots comprise, from left to right, the side view of the entire thermocouple and isometric views of each n- and p+ semiconductors

converged optimization for different boundary conditions and constraints with the penalty factors of $p_k = p_\sigma = 4$ and $p_\alpha = 1$.

The results in Fig. 16 show a preference toward combinations of column-like results for the lowest heat injection studied. These columns grow and merge with higher power constraints and heat injections. These shapes are related to the constant Peltier effect, which only depends on the material Seebeck coefficient gradient in the p–n connections and the decrease in overall thermal- and electrical conductivity with lower volume percentage. This ratio can be quantified through the figure-of-merit ($ZT = \frac{\alpha^2 \sigma}{k} T$), related to the efficiency of TEC devices.

The power constraint effect on the design is not so evident, as it can either increase or decrease the final volume percentage, see Fig. 14. This can be explained through the competing desired effects of low thermal and high electrical conductivity. For low power consumption, the Joule self-heating is not as important as providing good insulation to the warmer heat sink, resulting in lower volume designs. At the same time, at higher current flows, the optimizer minimizes the electrical resistance to reduce the device self-heating.

Finally, we can look at the case in Fig. 16 where the volume constraint becomes active for a volume constraint of 40 % and a power constraint of 30 mW. This result is dissimilar to the previous ones, finding internal cavities, lower contact surface, and an acute difference between both leg's thermal profiles, with the p-type leg noticeably warmer than its counterpart, given the worse electrical to thermal conductivity ratio of the p-type semiconductor.

5 Conclusion

This paper describes a procedure for the TO of thermocouples for cooling applications. Power constraints maintain optimal operational conditions, and volume constraints limit the material used in the final design.

The problem results in a non-convex design space influenced by the nonlinear thermoelectric equations, the power constraint,- and the material penalty coefficients. We propose an analytical model which allows us to visualize and understand the effect of different variables on the problem convergence with lower computational expense than FEM models. This study leads to the definition and recommendation of material penalty coefficients for SIMP TO of thermoelectrical devices. We give a recommendation of penalization coefficients following $p_k = p_\sigma > p_\alpha = 1$. The proposed combination of penalization coefficients allows for convergence without the need of volume constraints. Furthermore, from the combination of penalization coefficients studied, our recommendation provides the smallest dispersion of optimal objective values concerning the starting point for the optimization algorithm. Higher values for $p_k = p_\sigma$ lead to lower temperature objectives. However, these higher values also increase the nonlinearities affecting the problem convergence. Given the study on the penalization coefficients, we find that $p_k = p_\sigma = 4$ provides a good compromise.

The use of quadratic elements in combination with the selected penalty coefficients removes the need for TO filtering techniques to avoid checkerboarding. The use of quadratic elements also improves the nonlinear solver's FEM convergence for the thermoelectric equations at the cost of higher computational complexity. While filtering is not required, removing the optimizer's tendency to increase the density in electrically and thermally disconnected design regions in the converged results could be helpful and introduce a length scale. Following Lazarov and Sigmund (2011), these filters can be easily introduced into this formulation.

While the final converged solution results in full-density elements and disregards isolated material regions, we are still subject to manufacturing constraints. Historically, thermoelectric pellets are manufactured through sintering, limiting the complexity of the inner structures in thermoelectric pellets. However, new technologies, such as emerging trends in thermoelectric additive manufacturing, could alleviate these limitations. Nevertheless, manufacturability constraints are crucial to streamline the geometry and mitigate stress concentrations that negatively impact the reliability of the bulk-TEC design.

The initial geometry for the optimization also carries importance in the final optimized results. This study focuses on the bulk-TEC geometries due to their common use and previous experimental testing of the significance of their pellet geometry. However, this formulation could also benefit other current designs, including cylindrical, flat or wearable TEC designs with direct pn electrical connections without copper layers, see He et al. (2018). In some of these designs, introducing mechanical degrees of freedom can limit stresses due to differences in thermal expansion coefficients and allow for the design of elastic modules for wearable technologies. The use of multi-material formulations can also be helpful for the design of stacked semiconductors or meta-materials. Furthermore, the rise in porous thermoelectric materials research can improve TEC properties through microstructure optimization (Ijaz et al. 2024). These microstructures could be further integrated into the
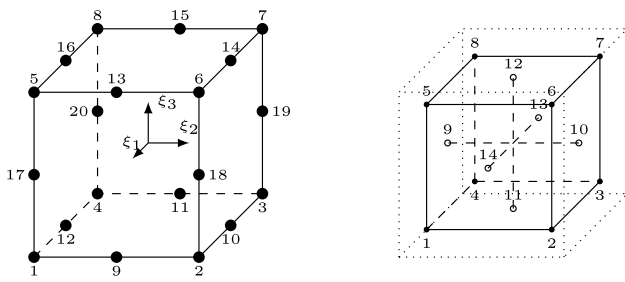
Fig. 17 Hexahedral 20 node element and 14 point reduced integration points with the superposed element in dotted lines

formulation through homogenization techniques for future thermoelectric materials.

While microstructures might play a large part in future thermoelectric modules, the material coefficients used assume a homogeneous medium, which might no longer be valid at small feature scales. Despite the interest of μ-TEC, this field still needs further research to facilitate device design and characterization methods Zhang et al. (2022). Another reason for revising the discrete thermoelectric equations is the case of TEC use under magnetic fields, which are known to modify thermoelectric coefficients. Although the research on the interplay of thermoelectric transport and magnetism is in its infancy (Liu et al. 2023), introducing the Nernst effect could lead to

more efficient devices. Furthermore, the material models used in this study keep the material coefficients constant with temperature to better understand the equivalent analytical problem. The results are only accurate for small temperature variations from the point where the material coefficients are calculated. Given the postprocessing performed using temperature-dependent material properties, we show that the optimization still provides better solutions than the original ones. However, we might still find better solutions with a formulation using temperature-dependent material properties during the optimization at the cost of higher computational costs and objectives with higher nonlinearities.

Overall, this paper provides solutions to convergence issues when attaining lower temperatures for TEC at lower volume geometries using TO. However, the material modeling and mechanical studies on the bulk- and other TEC designs should still be studied in further detail.

Serendipity 20 node element formulation

Serendipity 20 node elements are used in this work to reduce the complexity of the calculations while using second-order approximation polynomials. These elements and its reduced points of integration following a 14 point scheme developed in Hoit and Krishnamurthy (1995) are represented in Fig. 17.

In Fig. 17 we see the local coordinate system of the element in terms of ξ_i, the numbering system of each node. The location of each of these nodes and their associated shape function is represented in Table 2.

Finally, the integration of the element is performed in an internal hexahedron to the element. The integration points are then located in the internal hexahedron corners and face centers as defined in Table 3.

Analytical problem solution

The system of equations formed by Eqs. (43) and (44) can be solved, imposing a value of $V_0 = 0$, obtaining a value of T_c equal to,

Table 2 Node locations and shape functions for Hexahedral 20 node serendipity element

Node	ξ_1	ξ_2	ξ_3	Shape functions
1	−1	−1	−1	$(1-\xi_2)(1-\xi_3)(1-\xi_1)(-\xi_2-\xi_3-\xi_1-2)/8$
2	1	−1	−1	$(1+\xi_2)(1-\xi_3)(1-\xi_1)(\xi_2-\xi_3-\xi_1-2)/8$
3	1	1	−1	$(1+\xi_2)(1+\xi_3)(1-\xi_1)(\xi_2+\xi_3-\xi_1-2)/8$
4	−1	1	−1	$(1-\xi_2)(1+\xi_3)(1-\xi_1)(-\xi_2+\xi_3-\xi_1-2)/8$
5	−1	−1	1	$(1-\xi_2)(1-\xi_3)(1+\xi_1)(-\xi_2-\xi_3+\xi_1-2)/8$
6	1	−1	1	$(1+\xi_2)(1-\xi_3)(1+\xi_1)(\xi_2-\xi_3+\xi_1-2)/8$
7	1	1	1	$(1+\xi_2)(1+\xi_3)(1+\xi_1)(\xi_2+\xi_3+\xi_1-2)/8$
8	−1	1	1	$(1-\xi_2)(1+\xi_3)(1+\xi_1)(-\xi_2+\xi_3+\xi_1-2)/8$
9	0	−1	−1	$(1-\xi_2^2)(1-\xi_3)(1-\xi_1)/4$
10	1	0	−1	$(1+\xi_2)(1-\xi_3^2)(1-\xi_1)/4$
11	0	1	−1	$(1-\xi_2^2)(1+\xi_3)(1-\xi_1)/4$
12	−1	0	−1	$(1-\xi_2)(1-\xi_3^2)(1-\xi_1)/4$
13	−1	−1	0	$(1-\xi_2^2)(1-\xi_3)(1+\xi_1)/4$
14	1	−1	0	$(1+\xi_2)(1-\xi_3^2)(1+\xi_1)/4$
15	1	1	0	$(1-\xi_2^2)(1+\xi_3)(1+\xi_1)/4$
16	−1	1	0	$(1-\xi_2)(1-\xi_3^2)(1+\xi_1)/4$
17	0	−1	1	$(1-\xi_2)(1-\xi_3)(1-\xi^2)/4$
18	1	0	1	$(1+\xi_2)(1-\xi_3)(1-\xi^2)/4$
19	0	1	1	$(1+\xi_2)(1+\xi_3)(1-\xi^2)/4$
20	−1	0	1	$(1-\xi_2)(1+\xi_3)(1-\xi^2)/4$

Table 3 14 point integration scheme for a 20 node hexahedral element

Type	Integration point location		Weight
Corner points	$\xi_1 = \pm\,0.7587869106$		0.3351800554
	$\xi_2 = \pm\,0.7587869106$		
	$\xi_3 = \pm\,0.7587869106$		
Center points	$\xi_1 = \pm\,0.7958224257$	$\xi_2 = \xi_3 = 0$	0.8864265927
	$\xi_2 = \pm\,0.7958224257$	$\xi_1 = \xi_3 = 0$	
	$\xi_3 = \pm\,0.7958224257$	$\xi_1 = \xi_2 = 0$	

$$T_c = \frac{T_n}{T_d}, \tag{48}$$

$$
\begin{aligned}
T_n = k(&2\alpha\sigma V_f x_2^{2p_\sigma+p_k} x_1^{p_a+p_\sigma} - 4k x_2^{2p_k} x_1^{2p_a+p_\sigma} \\
&- 4\alpha^2\sigma T_h x_2^{2p_a+p_\sigma+p_k} x_1^{2p_a+p_\sigma} \\
&- 4\alpha^2\sigma T_h x_2^{p_k} x_1^{2(2p_a+p_\sigma)} + 2\alpha\sigma V_f x_2^{p_k} x_1^{3p_a+2p_\sigma} \\
&+ 4k x_2^{2p_a+p_\sigma+p_k} x_1^{p_k} \\
&\pm \alpha^2\sigma L x_2^{2(2p_a+p_\sigma)}(Sq) x_1^{p_k} + 4k x_2^{2p_a+p_\sigma} x_1^{2p_k} \\
&+ 2\alpha\sigma V_f x_2^{2p_a+p_\sigma} x_1^{p_a+p_\sigma+p_k} \\
&- 4\alpha^2\sigma T_h x_2^{2p_a+p_\sigma} x_1^{2p_a+p_\sigma+p_k} \\
&- 4k x_2^{p_k} x_1^{2p_a+p_\sigma+p_k} \\
&\pm 2\alpha^2\sigma L x_2^{2p_a+p_\sigma}(Sq) x_1^{2p_a+p_\sigma+p_k} \\
&+ 2\alpha\sigma V_f x_1^{3p_a+2p_\sigma+p_k} - 4\alpha^2\sigma T_h x_1^{4p_a+2p_\sigma+p_k} \\
&\pm \alpha^2\sigma L(Sq) x_1^{4p_a+2p_\sigma+p_k}),
\end{aligned}
\tag{49}
$$

$$
\begin{aligned}
T_d = 2\alpha^2\sigma(&x_1^{2p_a+p_\sigma} + x_2^{2p_a+p_\sigma})(-\alpha\sigma V_f(x_1^{2p_a+p_\sigma} \\
&+ x_2^{2p_a+p_\sigma})x_1^{p_a+p_\sigma} + 2\alpha^2\sigma T_h(x_1^{2p_a+p_\sigma} + x_2^{2p_a+p_\sigma}) \\
&x_1^{2p_a+p_\sigma} + k(2x_1^{2p_a+p_\sigma} x_2^{p_k} - 2x_1^{p_k} x_2^{2p_a+p_\sigma})),
\end{aligned}
\tag{50}
$$

with T_c providing 2 results to the system depending on the sign of the square root, S_q,

$$S_q = \sqrt{\frac{S_n}{S_d}}, \tag{51}$$

$$
\begin{aligned}
S_n = x_1^{-2p_k}(&\alpha\sigma V_f(x_1^{2p_a+p_\sigma} + x_2^{2p_a+p_\sigma})x_1^{p_a+p_\sigma} \\
&- 2\alpha^2\sigma T_h(x_1^{2p_a+p_\sigma} + x_2^{2p_a+p_\sigma})x_1^{2p_a+p_\sigma} \\
&+ 2k(x_1^{p_k} x_2^{2p_a+p_\sigma} - x_1^{2p_a+p_\sigma} x_2^{p_k}))^2 \\
&(4A\sigma^2 T_h^2(x_1^{2p_a+p_\sigma} + x_2^{2p_a+p_\sigma})^2\alpha^4 \\
&- 4A\sigma^2 T_h V_f(x_2^{2p_a+p_\sigma} x_1^{p_a+p_\sigma} + x_2^{p_a+p_\sigma} x_1^{2p_a+p_\sigma} \\
&+ x_1^{3p_a+2p_\sigma} + x_2^{3p_a+2p_\sigma})\alpha^3 \\
&+ \sigma(x_1^{2p_a+p_\sigma} + x_2^{2p_a+p_\sigma})(A\sigma(x_1^{p_\sigma} + x_2^{p_\sigma})V_f^2 \\
&+ 4Lq + 8AkT_h(x_1^{p_k} + x_2^{p_k}))\alpha^2 \\
&+ 4Ak^2(x_1^{p_k} + x_2^{p_k})^2),
\end{aligned}
\tag{52}
$$

$$S_d = A\alpha^4\sigma^2 k^2 L^2 \left(x_1^{2p_a+p_\sigma} + x_2^{2p_a+p_\sigma}\right)^4. \tag{53}$$

The other result we need to extract from the analytical formulation is the power consumption of the device which can be written as,

$$P = \sum |j_i A V_c|, \tag{54}$$

where the V_c value is evident noting that both electrical contacts, made by legs influenced by both x_i, will always have the same material properties overall and is written as,

$$V_c = \frac{V_f}{2}. \tag{55}$$

The current densities j_i are then equal for each leg with the same density variable with opposite signs,

$$j_1 = -j_4, \tag{56}$$

$$j_2 = -j_3. \tag{57}$$

The results for these current densities can be written as,

$$j_i = \frac{j_{ni}}{j_d}, \tag{58}$$

with the equations,

$$
\begin{aligned}
j_{n4} = x_1^{p_\sigma}(&-\alpha^2\sigma^2 V_f^2 x_2^{2(2p_a+p_\sigma)} x_1^{p_a+p_\sigma} \\
&+ 4\alpha^3\sigma^2 T_h V_f x_2^{2(2p_a+p_\sigma)} x_1^{2p_a+p_\sigma} \\
&+ 4\alpha\sigma k V_f x_2^{2p_a+p_\sigma+p_k} x_1^{2p_a+p_\sigma} \\
&+ 8\alpha^3\sigma^2 T_h V_f x_2^{2p_a+p_\sigma} x_1^{2(2p_a+p_\sigma)} \\
&+ 4\alpha\sigma k V_f x_2^{p_k} x_1^{2(2p_a+p_\sigma)} + 4\alpha^3\sigma^2 T_h V_f x_1^{3(2p_a+p_\sigma)} \\
&- 4\alpha^4\sigma^2 T_h^2 x_2^{2(2p_a+p_\sigma)} x_1^{3p_a+p_\sigma} - 4k^2 x_2^{2p_k} x_1^{3p_a+p_\sigma} \\
&- 8\alpha^2\sigma k T_h x_2^{2p_a+p_\sigma+p_k} x_1^{3p_a+p_\sigma} \\
&- 2\alpha^2\sigma^2 V_f^2 x_2^{2p_a+p_\sigma} x_1^{3p_a+2p_\sigma} - 8\alpha^4\sigma^2 T_h^2 x_2^{2p_a+p_\sigma} x_1^{5p_a+2p_\sigma} \\
&- 8\alpha^2\sigma k T_h x_2^{p_k} x_1^{5p_a+2p_\sigma} - \alpha^2\sigma^2 V_f^2 x_1^{5p_a+3p_\sigma} \\
&- 4\alpha^4\sigma^2 T_h^2 x_1^{7p_a+3p_\sigma} - 2\alpha\sigma k V_f x_2^{2(2p_a+p_\sigma)} x_1^{p_k} \\
&+ 4\alpha^2\sigma k T_h x_2^{2(2p_a+p_\sigma)} x_1^{p_a+p_k} \\
&+ 4k^2 x_2^{2p_a+p_\sigma+p_k} x_1^{p_a+p_k} \pm \alpha^2\sigma k L x_2^{2(2p_a+p_\sigma)}(S_q) x_1^{p_a+p_k} \\
&- 4k^2 x_2^{p_k} x_1^{3p_a+p_\sigma+p_k} \\
&\pm 2\alpha^2\sigma k L x_2^{2p_a+p_\sigma}(S_q) x_1^{3p_a+p_\sigma+p_k} \\
&+ 2\alpha\sigma k V_f x_1^{4p_a+2p_\sigma+p_k} \\
&- 4\alpha^2\sigma k T_h x_1^{5p_a+2p_\sigma p_k} \pm \alpha^2\sigma k L(S_q) x_1^{5p_a+2p_\sigma+p_k} \\
&+ 4k^2 x_2^{2p_a+p_\sigma} x_1^{p_a+2p_k}),
\end{aligned}
\tag{59}
$$

and,

$$
\begin{aligned}
j_{n2} = x_2^{p_\sigma}(&4\alpha^4\sigma^2 T_h^2 x_1^{3(2p_\alpha+p_\sigma)} x_2^{p_\alpha} \\
&- 2\alpha^3\sigma^2 T_h V_f x_1^{5p_\alpha+3p_\sigma} x_2^{p_\alpha} \\
&- 2\alpha\sigma k V_f x_1^{3p_\alpha+2p_\sigma+p_k} x_2^{p_\alpha} \\
&+ 4\alpha^2\sigma k T_h x_1^{4p_\alpha+2p_\sigma+p_k} x_2^{p_\alpha} \\
&\mp \alpha^2\sigma k L x_1^{4p_\alpha+2p_\sigma+p_k}(S_q) x_2^{p_\alpha} \\
&- 4\alpha^3\sigma^2 T_h V_f x_1^{2(2p_\alpha+p_\sigma)} x_2^{2p_\alpha+p_\sigma} \\
&+ 2\alpha^2\sigma^2 V_f^2 x_1^{3p_\alpha+2p_\sigma} x_2^{2p_\alpha+p_\sigma} \\
&+ 2\alpha\sigma k V_f x_1^{2p_\alpha+p_\sigma+p_k} x_2^{2p_\alpha+p_\sigma} \\
&+ \alpha^2\sigma^2 V_f^2 x_1^{p_\alpha+p_\sigma} x_2^{2(2p_\alpha+p_\sigma)} \\
&- 2\alpha^3\sigma^2 T_h V_f x_1^{2p_\alpha+p_\sigma} x_2^{2(2p_\alpha+p_\sigma)} \\
&+ 2\alpha\sigma k V_f x_1^{p_k} x_2^{2(2p_\alpha+p_\sigma)} \\
&+ 8\alpha^4\sigma^2 T_h^2 x_1^{2(2p_\alpha+p_\sigma)} x_2^{3p_\alpha+p_\sigma} \\
&- 4\alpha^3\sigma^2 T_h V_f x_1^{3p_\alpha+2p_\sigma} x_2^{3p_\alpha+p_\sigma} \\
&- 4k^2 x_1^{2p_k} x_2^{3p_\alpha+p_\sigma} \\
&- 2\alpha\sigma k V_f x_1^{p_\alpha+p_\sigma+p_k} x_2^{3p_\alpha+p_\sigma} \\
&\mp 2\alpha^2\sigma k L x_1^{2p_\alpha+p_\sigma+p_k}(S_q) x_2^{3p_\alpha+p_\sigma} \\
&- 2\alpha^3\sigma^2 T_h V_f x_1^{p_\alpha+p_\sigma} x_2^{5p_\alpha+2p_\sigma} \\
&+ 4\alpha^4\sigma^2 T_h^2 x_1^{2p_\alpha+p_\sigma} x_2^{5p_\alpha+2p_\sigma} \\
&- 4\alpha^2\sigma k T_h x_1^{p_k} x_2^{5p_\alpha+2p_\sigma} \mp \alpha^2\sigma k L x_1^{p_k}(S_q)) x_2^{5p_\alpha+2p_\sigma} \\
&- 2\alpha\sigma k V_f x_1^{2(2p_\alpha+p_\sigma)} x_2^{p_k} \\
&+ 8\alpha^2\sigma k T_h x_1^{2(2p_\alpha+p_\sigma)} x_2^{p_\alpha+p_k} \\
&- 2\alpha\sigma k V_f x_1^{3p_\alpha+2p_\sigma} x_2^{p_\alpha+p_k} \\
&+ 4k^2 x_1^{2p_\alpha+p_\sigma+p_k} x_2^{p_\alpha+p_k} \\
&- 2\alpha\sigma k V_f x_1^{2p_\alpha+p_\sigma} x_2^{2p_\alpha+p_\sigma+p_k} \\
&- 2\alpha\sigma k V_f x_1^{p_\alpha+p_\sigma} x_2^{3p_\alpha+p_\sigma+p_k} \\
&+ 8\alpha^2\sigma k T_h x_1^{2p_\alpha+p_\sigma} x_2^{3p_\alpha+p_\sigma+p_k} \\
&- 4k^2 x_1^{p_k} x_2^{3p_\alpha+p_\sigma+p_k} \\
&+ 4k^2 x_1^{2p_\alpha+p_\sigma} x_2^{p_\alpha+2p_k} \\
&- 2\alpha^3\sigma^2 T_h V_f x_1^{3(2p_\alpha+p_\sigma)} + \alpha^2\sigma^2 V_f^2 x_1^{5p_\alpha+3p_\sigma}),
\end{aligned}
\tag{60}
$$

characterizing all current density flow numerators and with common denominator for all current densities,

$$
\begin{aligned}
j_d = 2\alpha L(&x_1^{2p_\alpha+p_\sigma} + x_2^{2p_\alpha+p_\sigma})(-\alpha\sigma V_f(x_1^{2p_\alpha+p_\sigma} + x_2^{2p_\alpha+p_\sigma}) \\
&x_1^{p_\alpha+p_\sigma} + 2\alpha^2\sigma T_h(x_1^{2p_\alpha+p_\sigma} + x_2^{2p_\alpha+p_\sigma})x_1^{2p_\alpha+p_\sigma} \\
&+ k(2x_1^{2p_\alpha+p_\sigma} x_2^{p_k} - 2x_1^{p_k} x_2^{2p_\alpha+p_\sigma})).
\end{aligned}
\tag{61}
$$

Declarations

References

Bendsøe MP, Kikuchi N (1988) Generating optimal topologies in structural design using a homogenization method. Comput Methods Appl Mech Eng 71(2):197–224. https://doi.org/10.1007/s0041 90050248

Bornheim A, Lustermann W, Stachon K, Reales Gutiérrez G, Benaglia A, De Guio F, Ghezzi A, Lucchini MT, Malberti M, Palluotto S, Tabarelli De Fatis T, Benettoni M, Carlin R, Tosi M, Rossin R, Meridiani P, Paramatti R, Santanastasio F, Silva JC, Varela J, Heering A, Karneyeu A, Musienko Y, Wayne M, Anderson T, Cox B, Perez Lara CE, Ledovskoy A, White S, Schmidt I (2023) Integration of thermo-electric coolers into the CMS MTD SiPM arrays for operation under high neutron fluence. J Instrum. https://doi.org/10.1088/1748-0221/18/08/P08020, arXiv:2306.00818

Fabiá¡n-Mijangos A, Min G, Alvarez-Quintana J (2017) Enhanced performance thermoelectric module having asymmetrical legs. Energy Convers Manag 148:1372–1381. https://doi.org/10.1016/j.enconman.2017.06.087. https://www.sciencedirect.com/science/article/pii/S0196890417306325

Fanni M, Shabara MN, Alkalla MG (2013) A comparison between different topology optimization methods. Egypt Knowl Bank. https://doi.org/10.21608/BFEMU.2020.103788

Furuta K, Izui K, Yaji K, Yamada T, Nishiwaki S (2017) Level setbased topology optimization for the design of a peltier effect

thermoelectric actuator. Struct Multidisc Optim 55(5):1671–1683. https://doi.org/10.1007/s00158-016-1609-9

Goupil C, Seifert W, Zabrocki K, Müller E, Snyder GJ (2011) Thermodynamics of thermoelectric phenomena and applications. Entropy 13(8):1481–1517. https://doi.org/10.3390/e13081481. https://www.mdpi.com/1099-4300/13/8/1481

He R, Schierning G, Nielsch K (2018) Thermoelectric devices: a review of devices, architectures, and contact optimization. Adv Mater Technol 3(4):1700256. https://doi.org/10.1002/admt.201700256

Hoit M, Krishnamurthy K (1995) A 14-point reduced integration scheme for solid elements. Comput Struct 54(4):725–73. https://doi.org/10.1016/0045-7949(94)00360-F. https://www.sciencedirect.com/science/article/pii/004579499400360F

Hu X, Takazawa H, Nagase K, Ohta M, Yamamoto A (2015) Three-dimensional finite-element simulation for a thermoelectric generator module. J Electron Mater 44(10):3637–3645. https://doi.org/10.1007/s11664-015-3898-y

Ibeagwu OI (2019) Modelling and comprehensive analysis of tegs with diverse variable leg geometry. Energy 180:90–106. https://doi.org/10.1016/j.energy.2019.05.088. https://www.sciencedirect.com/science/article/pii/S036054421930965X

Ijaz U, Siyar M, Park C (2024) The power of pores: review on porous thermoelectric materials. RSC Sustain 00:1–19. https://doi.org/10.1039/d3su00451a

IRENA, IEA, REN21 (2020) Renewable energy-heating and cooling. IRENA, OECD/IEA and REN21

Lazarov BS, Sigmund O (2011) Filters in topology optimization based on Helmholtz-type differential equations. Int J Numer Methods Eng 86(6):765–781. https://doi.org/10.1002/nme.3072

LeBlanc S, Yee SK, Scullin ML, Dames C, Goodson KE (2014) Material and manufacturing cost considerations for thermoelectrics. Renew Sustain Energy Rev 32:313–327. https://doi.org/10.1016/j.rser.2013.12.030. https://www.sciencedirect.com/science/article/pii/S1364032113008447

Lee HS (2013) The Thomson effect and the ideal equation on thermoelectric coolers. Energy 56:61–69. https://doi.org/10.1016/j.energy.2013.04.049

Liu Q, Li G, Zhu H, Zhao H (2022) Micro thermoelectric devices: from principles to innovative applications. Chin Phys B 31(4):047204. https://doi.org/10.1088/1674-1056/ac5609

Liu Q, Wei F, Li G, Kan Z, Yang J, Zhu H, Wang B, Zhao H (2022) Highly efficient thermoelectric air conditioner with kilowatt capacity realized by ground source heat-exchanging system. iScience 25(5):104296. https://doi.org/10.1016/j.isci.2022.104296

Liu S, Chen M, Fu C, Zhu T (2023) The interplay of magnetism and thermoelectricity: a review. Adv Phys Res 2(9):2300015. https://doi.org/10.1002/apxr.202300015

Lundgaard C, Sigmund O (2018) A density-based topology optimization methodology for thermoelectric energy conversion problems. Struct Multidisc Optim 57(4):1427–1442. https://doi.org/10.1007/s00158-018-1919-1

Mativo J, Hallinan K (2019) Development of compliant thermoelectric generators (TEGs) in aerospace applications using topology optimization. Energy Harvest Syst 4(2):87–105. https://doi.org/10.1515/ehs-2016-0017

Mativo J, Hallinan K, George U, Reich G, Steininger R (2020) Topology optimized thermoelectric generator: a parametric study. Energy Harvest Syst 7(2):33–53. https://doi.org/10.1515/ehs-2021-0002

Maurya ES (2020) Liquid cooling system and air cooling system in data center: a comparison. Int J Res Appl Sci Eng Technol 8(11):548–550. https://doi.org/10.22214/ijraset.2020.32226

Peltier JCA (1834) Nouvelles experiences sur la caloricite des courants electriques. In: Annales de chimie et de physique, LVI. LVI, pp 371–386

Pérez-Aparicio JL, Taylor RL, Gavela D (2007) Finite element analysis of nonlinear fully coupled thermoelectric materials. Comput Mech 40(1):35–45. https://doi.org/10.1007/s00466-006-0080-7

Riffat S, Ma X (2003) Thermoelectrics: a review of present and potential applications. Appl Therm Eng 23(8):913–93. https://doi.org/10.1016/S1359-4311(03)00012-7. https://www.sciencedirect.com/science/article/pii/S1359431103000127

Sandoz-Rosado EJ, Weinstein SJ, Stevens RJ (2013) On the Thomson effect in thermoelectric power devices. Int J Therm Sci 66:1–7. https://doi.org/10.1016/j.ijthermalsci.2012.10.018. https://www.sciencedirect.com/science/article/pii/S129007291200292X

Sardan O, Petersen DH, Mølhave K, Sigmund O, Bøggild P (2008) Topology optimized electrothermal polysilicon microgrippers. Microelectron Eng 85(5):1096–1099. https://doi.org/10.1016/j.mee.2008.01.049. https://www.sciencedirect.com/science/article/pii/S0167931708000361. Proceedings of the Micro- and Nano-Engineering 2007 Conference

Shittu S, Li G, Zhao X, Ma X (2020) Review of thermoelectric geometry and structure optimization for performance enhancement. Appl Energy 268:115075. https://doi.org/10.1016/j.apenergy.2020.115075. https://www.sciencedirect.com/science/article/pii/S0306261920305870

Sigmund O, Maute K (2013) Topology optimization approaches: a comparative review. Struct Multidisc Optim 48(6):1031–1055. https://doi.org/10.1007/s00158-013-0978-6

Soprani S, Haertel JH, Lazarov BS, Sigmund O, Engelbrecht K (2016) A design approach for integrating thermoelectric devices using topology optimization. Appl Energy 176(June):49–64. https://doi.org/10.1016/j.apenergy.2016.05.024

Svanberg K (1987) The method of moving asymptotes–a new method for structural optimization. Int J Numer Methods Eng 24:359–373

Takezawa A, Kitamura M (2012) Geometrical design of thermoelectric generators based on topology optimization. Int J Numer Methods Eng 90(11):1363–1392. https://doi.org/10.1002/nme.3375

Xu X, Wu Y, Zuo L, Chen S (2019) Multimaterial topology optimization of thermoelectric generators. In: Proceedings of the ASME Design Engineering Technical Conference 2A-2019 (September 2021). https://doi.org/10.1115/DETC2019-97934

Yago D, Cante J, Lloberas-Valls O, Oliver J (2021) Topology optimization methods for 3D structural problems: a comparative study. Arch Comput Methods Eng. https://doi.org/10.1007/s11831-021-09626-2. arXiv:2108.03146

Yang D, Yang P (2010) Numerical instabilities and convergence control for convex approximation methods. Nonlinear Dyn 61(4):605–62. https://doi.org/10.1007/s11071-010-9674-x

Zhang Q, Deng K, Wilkens L, Reith H, Nielsch K (2022) Micro-thermoelectric devices. Nat Electron 5(6):333–347. https://doi.org/10.1038/s41928-022-00776-0

Zhao D, Tan G (2014) A review of thermoelectric cooling: materials, modeling and applications. Appl Therm Eng 66(1):15–24. https://doi.org/10.1016/j.applthermaleng.2014.01.074. https://www.sciencedirect.com/science/article/pii/S1359431114000854